Scaling mean velocity and Reynolds stress of a turbulent boundary layer submitted to an adverse pressure gradient

J.M. Foucaut[a], C. Arrive[a], C. Cuvier[a], J.C. Monnier[a], C.E. Willert[b], J. Soria[c]

[a] *Univ. Lille, CNRS, ONERA, Centrale Lille, Arts et Metiers ParisTech, UMR9014, Laboratoire de Mécanique des Fluides de Lille - Kampé de Fériet (LMFL), F-59000 Lille, France.*

[b] *DLR Institute of Propulsion Technology, Köln, Germany*

[c] *Monash University, LTRAC, Department of Mechanical and Aerospace Engineering, Clayton Campus, Melbourne, Australia*

Abstract

Despite considerable progress in understanding zero pressure gradient boundary layers, turbulence in adverse pressure gradient (APG) boundary layers remains less well understood, particularly in high Reynolds number flows. Unfavorable pressure gradient regions are commonly encountered in industrial applications, but turbulence models often lack the physical basis necessary for reliable predictions in these flows. This study focuses on analyzing the effects of adverse pressure gradient on boundary layer scaling, essential for predicting flow characteristics and validating turbulence models. Building on recent advances in experimental methods and using large-scale particle image velocimetry (PIV), the research aims to provide an analysis of turbulent boundary layer flows in APG. Experiments have been carried out in a wind tunnel using inclined plates to induce pressure gradients at an angle of $-8°$, complementing an existing database obtained at $-5°$ (see Cuvier et al., 2017) and offering new insights into flow behavior. An analysis of the literature has enabled the authors to compare various scaling approaches and to propose a scaling that is suitable for both mean velocity and Reynolds stress.

Keywords: Turbulent boundary layer, Adverse pressure gradient, Scaling, Particle image velocimetry

1. Introduction

The study of the turbulent boundary layer (TBL) under adverse pressure gradient (APG) conditions remains a key challenge in aerodynamics due to the complex nature of flow behavior in such regions. APG flows are characterized by a decelerating flow field where the pressure increases in the direction of the flow, leading to an adverse pressure gradient. These conditions not only induce higher turbulence levels but also have significant implications for flow separation, drag and energy dissipation, making them a critical area of study for both fundamental fluid mechanics and applied engineering problems.

Since the work of Prandtl and von Kármán, research into the scaling of turbulent boundary layers influenced by pressure gradients has been extensively studied, notably in the 1950s by Rotta (1950), Clauser (1954, 1956), Coles (1956) and Townsend (1956), among others. In these studies, representations were often experimentally tested on the databases of Ludwig and Tillman (1950) and Clauser (1954). Not only the amount of data, but also the flow range was limited, and the lack of knowledge of certain parameters such as wall friction velocity was problematic both in boundary layers without pressure gradient (ZPG) and even more so under the effect of an adverse pressure gradient (APG). Later, Townsend (1961) and Perry (1966) proposed new developments for the near-wall region around the equilibrium boundary layer concept, revisited by Mellor and Gibson (1966). In 1968, at the Stanford Conference, Coles (1968) pointed out that the available data were inadequate in scope and quality. It was reiterated that there is an important and continuing need for more complete and accurate experimental data. Indeed, experiments on TBL subjected to pressure gradients were rare at the time. Nevertheless, a few experiments were carried out which are briefly presented in Maciel et al. (2006).

However, the definition of interesting cases for TBL subjected to pressure gradients has been much discussed over the last 20 years, and has sometimes been the subject of controversy. Although the theories proposed by Rotta (1950) and Clauser (1954) are still the most common definitions of self-similar equilibrium boundary layers for TBL, many advances have been made in their definitions. The various possibilities are based on different assumptions about the type of self-similarity to be achieved. Certain similarity conditions are sometimes more difficult to satisfy (see Castillo and George, 2001 and Maciel et al., 2006). Questions remain open, such as the choice of length and

velocity scales that characterize the outer layer of TBL and more particularly when they are subjected to a pressure gradient (see Maciel et al., 2018).

For turbulent flows limited to walls with zero pressure gradient, wall turbulence is characterized by a single velocity scale, the friction velocity, u_τ, and two length scales, one associated with the external flow, δ, the thickness of the boundary layer at 99% of the external velocity, and the other associated with the near-wall region where viscous actions are important, often $\delta_\nu = \nu/u_\tau$, where ν is the kinematic viscosity of the fluid, respectively. The ratio between these two length scales is called the friction Reynolds number, $Re_\tau = \delta^+ = \delta u_\tau/\nu$, which also represents the range of scales in a TBL. The asymptotic connection between the inner zone and the outer flow gives the classical logarithmic wall law, which remains one of the theoretical foundations for turbulent flows close to a wall. Chen et al. (2023) question the presence of a logarithmic law and propose a universal velocity transformation that restores a behavior close to the wall law, even in the presence of strong gradients.

The universality of the mean velocity profile of the inner layer has been the subject of numerous studies (see e.g. Pirozzoli and Smits, 2023). For external flows, part of the uncertainty in scaling is often related to the length scale, as the boundary layer thickness is not well defined. This led Rotta (1950) and Clauser (1954) to propose the displacement thickness as a relevant length scale. Although the universality of the outer zone is often limited due to a lack of total similarity, the friction velocity is often considered the appropriate velocity scale (see Nagib and Chauhan, 2008 and Panton, 2005). Nevertheless, arguments based on conditions required for self-similarity solutions of the boundary layer equations suggest that external velocity might be a possible alternative (Castillo and George, 2001; Kitsios et al., 2017). Physical arguments led Zagarola and Smits (1998) to identify an alternative velocity scale as the difference between the external velocity and the bulk velocity.

To validate the boundary layer similarity study, high-quality boundary layer data at high Reynolds numbers and for different pressure gradient conditions are required. Such data are beginning to become available both experimentally and numerically. On the experimental side, large-scale APG TBL have only been recently measured with high-resolution particle image velocimetry and particle tracking velocimetry by Cuvier et al. (2017) and Knopp et al. (2015) and with hot wire anemometry by Romero et al. (2022) with Re_θ reaching 23,000, 26,000 and 41,000, respectively. Clauser's β pa-

rameters for pressure gradients are of the order of 2-3 and 1-2 for Cuvier et al. (2017) and Romero et al. (2022), respectively. Two recent DNS have also achieved relatively high Reynolds numbers, although not as high as those of the aforementioned experiments. These are the DNS of a strongly decelerating TBL by Gungor et al. (2017) with Re_θ reaching 8000, and the self-similar APG TBL at the verge of separation by Kitsios et al. (2017) with a self-similar region of Re_θ from 10,000 to 12,300, and a very high Clauser β parameter of 39.

Despite the vast amount of existing work, validation of the various theoretical proposals is still required in the case of a TBL subjected to an adverse pressure gradient and, consequently, analysis of new databases is necessary to validate the theoretical foundations. Furthermore, there seems to be no agreement on the scales to be used, which is the main subject of this paper. However, known scales such as those of Clauser (1954), George and Castillo (1997), Zagarola and Smits (1998), Pirozzoli and Smits (2023) yield recognized results for the mean velocity profile at least in ZPG. Romero et al. (2022) has shown that when scaling Reynolds stresses in the inner zone of the TBL in APG, the pressure gradient in the velocity scale must be taken into account. They also showed that the history of the flow prior to its deceleration is important in the search for universality, which was observed in previous studies (see Castillo and George, 2001; Bobke et al., 2017). The question of choosing the right scales is crucial. Klewicki et al. (2024) point out that the right formalism must take into account the inertia-gradient interaction in the momentum balance. Han et al. (2024) have proposed a generalization of the Zagarola-Smits scaling, extended to all Reynolds stress components, ensuring better homogenization of profiles in the outer region. Vinuesa et al. (2016) insist on the robustness of a criterion based on the disappearance of the mean velocity gradient to define the boundary layer.

In the present study, we supplement the database of Cuvier et al. (2017) with a new set of experiments carried out under the same in-flow conditions but with different pressure gradients, so as to be able to emphasize the influence of this parameter without altering the flow history. We also propose to compare the most classical as well as the most recent scaling by Pirozzoli and Smits (2023) and Romero et al. (2022) in the case of the outer zone first on mean velocity profiles and then on the Reynolds stresses. Furthermore, we propose a new set of parameters that builds on these two studies to arrive at a Reynolds number-independent similarity.

Through this comparison, a new contribution to the ongoing effort to

develop a more universal scaling framework for APG TBL is provided. This scaling not only improves the understanding of the underlying physics of APG flows but also provides a more accurate predictive tool for real-world applications, such as in aerodynamic design and energy-efficient transport systems.

2. Databases

All experiments were conducted in the boundary layer wind tunnel of the Laboratoire de Mécanique des Fluides de Lille (LMFL). Fig. 1 provide a front and top view of the LMFL TBL wind tunnel, which features a test section length of 20.6 m. The test section is transparent on all sides with high-quality 10 mm glass, allowing for complete optical access. The cross-section measures 2 m in width and 1 m in height, with a free-stream velocity range from 1 to 9.4 m/s, measured 100 mm downstream of the test section entrance. The wind tunnel can operate in a closed-loop configuration with temperature control or be opened to the outside.

In the closed-loop setup, the free-stream velocity is maintained within $\pm 0.5\%$, and the temperature within $\pm 0.15^\circ$ C. The boundary layer is tripped at the tunnel entrance using a 4 mm spanwise cylinder secured with silicon on the bottom wall, followed by 93 mm of Grit 40 sandpaper (mean roughness 425 μm). The boundary layer developing on the top wall is also initiated with a 93 mm wide spanwise strip of Grit 40 sandpaper. All glass surfaces and the bottom wall are aligned to ensure no step exceeds 0.1 mm (equivalent to 2^+ at maximum velocity). Additionally, the top, bottom and lateral walls are adjusted to be perfectly parallel, with deviations of less than $\pm 0.1^\circ$.

2.1. The EuHIT -5° experiment

The EuHIT -5° experiment was carried out in the frame of the European Project EuHIT with full details provided in Cuvier et al. (2017). For this experiment, the wind tunnel was used in the closed loop configuration and a specifically designed ramp model, approximately 7 m long, was installed on the bottom wall (see Fig. 2). The model used is the LML-AVERT ramp (Cuvier et al., 2014) on which the final section was replaced by a 3.5 m long plate inclined at a -5° angle with respect to the wind tunnel floor (in red in Fig. 2), with the aim of creating a constant adverse pressure gradient. The ramp's leading edge was located 9.4 m downstream from the entry of the test section. As shown in Fig. 2, following the contraction, which has

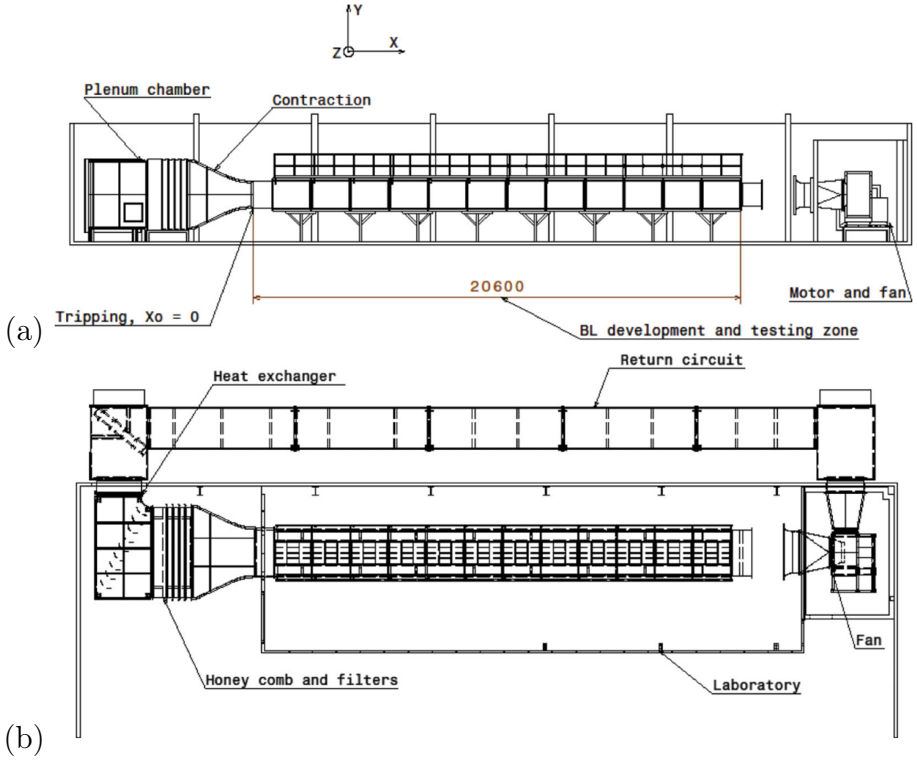

Figure 1: Front (a) and top view (b) of the LMFL wind tunnel.

a contraction ratio of 0.75, a flat plate measuring 2.14 m is positioned at an angle of +1.5° relative to the wind tunnel floor. The experiments were carried out for two inlet velocities of the wind tunnel, 5 m/s and 9 m/s, in order to have two Reynolds number ranges along the APG plate.

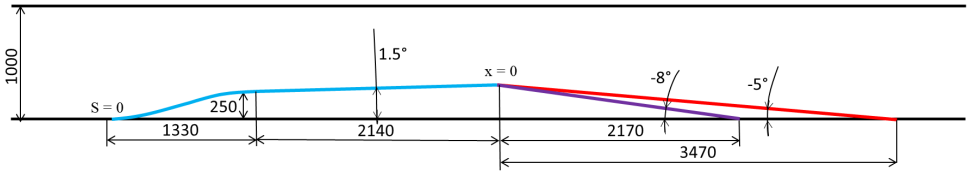

Figure 2: Sketch of the ramp model in the wind tunnel slope at −5° in red and −8° in purple.

To capture the flow in the APG region a large field 2D 2C PIV setup, based on stitched multi-camera configuration enabled the acquisition of ve-

locity field data over a 3.5 m long and 25 cm high domain as described in Cuvier et al. (2017). This was achieved by mounting 16 sCMOS cameras on the side of the wind tunnel, each with a field of view of 230 mm along the wall and 273 mm in the wall normal direction. To assure a continuous measurement domain, an overlap region around 10 to 20 mm was used between adjoining cameras. The domain was illuminated by a light sheet introduced through a narrow slit and 45° mirror at the downstream end of the APG ramp. The exceptional beam characteristics of the LMFL BMI YAG laser system ensured a light sheet thickness of 1 mm across the 3.5 m wide field of view.

To achieve a more precise characterization of the very near-wall region in the APG TBL, high magnification and high repetition 2D 2C PIV experiments were performed at three locations within the APG region identified as station (1), (3), and (4) as can be seen in Fig. (10) of Cuvier et al. (2017). These measurement points are situated 0.483 m, 1.733 m, and 2.358 m downstream of the beginning of the APG region, corresponding to $s = 3.983$ m, 5.233 m, and 5.858 m, respectively, where s is the curvilinear abscissa along the ramp, with the leading edge of the ramp set as origin (see Fig. 2). The friction velocity at the respective stations was determined using a single-line cross-correlation approach introduced by Willert (2015). Correlating wall-parallel rows of pixels from temporally adjacent PIV recordings provides instantaneous displacement estimates along the direction of the row. This is repeated for different wall distances (e.g. pixel rows) yielding an instantaneous displacement profile. A linear fit for displacement data within the viscous sublayer ($y^+ \leq 5$) results in an estimate of the instantaneous wall-shear rate at the given time-step.

2.2. The joint LMFL-ONERA −8° experiment

The joint LMFL-ONERA −8° experiment was carried out as part of an internal research project of ONERA. This experiment is a modification of the previously described setup with the primary objective of increasing the pressure gradient by replacing the original −5° plate at the end of the ramp with a −8° plate (in purple in Fig. 2). The wind tunnel setup and the ramp design remained unchanged, except for the final section, where a 2.2 m long plate was inclined at −8° relative to the wind tunnel floor. Moreover, the inlet velocities were identical to those of the EuHIT experiment, ensuring consistent flow history upstream and allowing the study of the pressure gradient's effect on the flow.

The PIV setup closely mirrors that of the EuHIT campaign, following the methods outlined in Cuvier et al. (2017). For this experiment, 10 cameras were mounted to capture a large field of view in the APG region, as illustrated in Fig. 3. Cameras 1 through 5 were equipped with 105 mm macro lenses. Camera 6 was fitted with a 60 mm lens positioned closer to the tunnel side wall to avoid the shadow of the wind tunnel side pillars (see Fig. 3), and cameras 7 through 10 used 105 mm non-macro lenses. The distance from the bench to the glass was maintained at 770 mm. The glass-to-front-lens distances were as follows: cameras 1 to 5 at 690 mm, camera 6 at 10 mm, and cameras 7 to 10 at 730 mm. All cameras were set with an f-number (f#) of 4, except for camera 10 (camera 1 located the furthest upstream), which had an f-number of 3.5. The light sheet was generated using the same specific set-up as for the EuHIT experiment. The analysis was done by means of a grid-refining, multiple-pass cross-correlation algorithm (Willert and Gharib, 1991; Soria, 1996) employing image deformation (Scarano, 2002) at the final pass with a 24×24 pixel interrogation window. Fig. 5 shows examples of mean streamwise velocity field normalized by U_∞ at: (a) $U_\infty = 5$ m/s and (b) $U_\infty = 9$ m/s. Visually the two recovered velocity fields are very similar and are free from discontinuities or spurious regions.

As in the EuHIT campaign, three stations were established to achieve a more detailed characterization of the near-wall region as in Cuvier et al. (2017). These stations — (1), (2), and (3) — were respectively located at 0.485 m, 1.204 m, and 1.774 m from the start of the APG region, corresponding to curvilinear positions of $s = 3.985$ m, 4.704 m, and 5.274 m. For this experiment a high speed camera (Vision Resarch, Phantom V2640) operating at 40 kHz with the active sensor size limited to 208×2048 pixel. In order to resolve the viscous sublayer the flow was imaged at a magnification of 0.86 with a 300 mm lens coupled to a 2X teleconverter. Illumination was provided by a high speed laser (Innolas Blizz 30 W). The lens aperture was set at $f/8$ to obtain particle image size of about 2 pixels to optimize the accuracy (Foucaut et al., 2003) and a displacement of about 20 pixels in the upper part of the field of view was selected to obtain both a high dynamic range of the turbulent fluctuations with high precision and low uncertainty close to the wall. The analysis was also done with a grid-refining, multiple-pass cross-correlation approach (Willert and Gharib, 1991; Soria, 1996). The images were analysed twice with a modified version of MatPIV at LMFL. The first by means of 24×24 pixels interrogation windows to resolve the turbulent profiles near the wall and the second by means of rectangular 48×8

pixels interrogation windows to resolve the near wall gradient of the viscous sublayer from which the skin friction is determined. For the final pass, image deformation was used to improve the measurement of the gradient and thus, the quality of the data (Scarano, 2002; Lecordier and Westerweel, 2004).

Table 1 summarizes the main parameters used for PIV recording in the different experiments.

Figure 3: Photograph of the camera setup for the ONERA APG TBL experiment.

Figure 4: Photograph of the laser setup for the ONERA APG TBL experiment.

3. Comparison between the experiments

3.1. Pressure coefficient and its gradient

For both datasets, pressure measurements were made along the ramp at 22 sections in the streamwise direction with a digital manometer 'FCO 560'. For each pressure tap, the data is sampled for 80 seconds at a frequency of

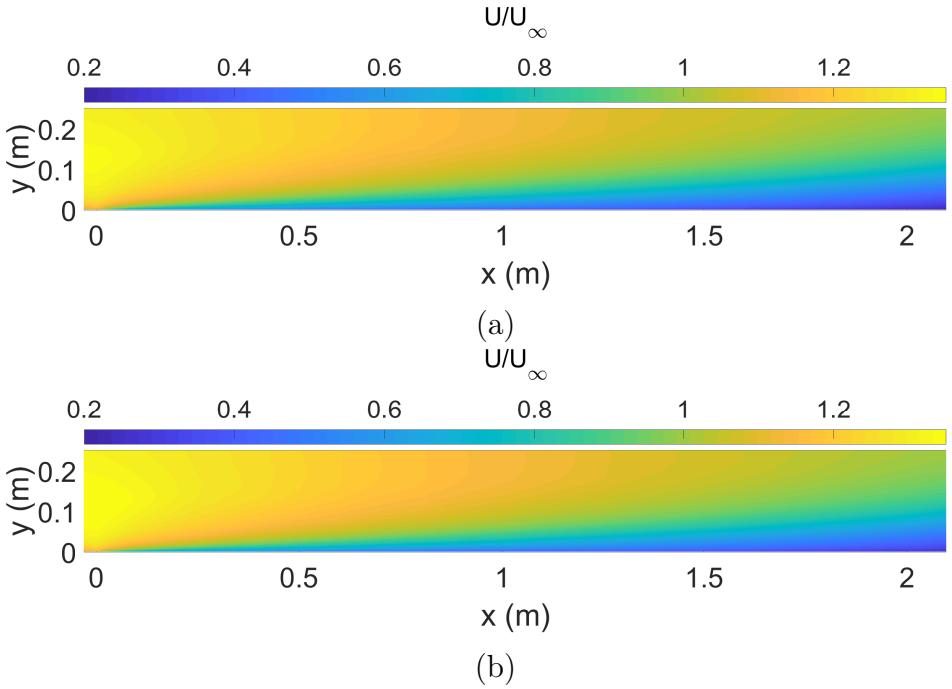

Figure 5: Examples for 2D field of the mean streamwise velocity for a ramp angle of $-8°$ at a) $U_\infty = 5\,\mathrm{m/s}$ and b) $U_\infty = 9\,\mathrm{m/s}$.

2 Hz. The reference pressure used to measure the differential pressure is at the transition between the contraction and the FPG sections. These values are represented using pressure coefficient defined in Eq. (1). The free-stream velocity is measured at the inlet of the test section.

$$C_p = \frac{\Delta P}{\frac{1}{2}\rho U_\infty^2} \tag{1}$$

Fig. 6 shows surface pressure coefficient over the ramp along the stream-wise direction for both experiments and the two free-stream velocities $U_\infty = 5$ m/s and 9 m/s while Fig. 7 shows the corresponding surface pressure gradient distributions. The horizontal axis represents the curvilinear coordinates s along the ramp surface in mm with $s = 0$ being the leading edge of the ramp (see Fig. 2).

As the flow moves from the leading edge downstream, it accelerates through the contraction section, causing the pressure coefficient C_p to decrease progressively. At the end of the contraction, a suction dip appears,

Experiment	Slope α	FOV (m×m)	Dt (px)	IW (px×px)	IW (mm×mm)	Vect field size	Number of samples	Frequency (Hz)
Large field streamwise 2D 2C PIV	$-5°$	3.46 x 0.255	14	24 x 24	2.56 x 2.56	3250 x 238	30 000	4
Large field streamwise 2D 2C PIV	$-8°$	2.16 x 0.255	14	24 x 24	2.55 x 2.55	2048 x 242	30 000	4
Time-resolved high magnification PIV	$-5°$	0.003 x 0.019 0.003 x 0.038	25	32 x 8	0.8 x 0.2	5 x 640 5 x 1280	10 000 50 000	100 500
Time-resolved high magnification PIV	$-8°$	0.0032 x 0.032 0.0032 x 0.0064	25	24 x 24 48 x 8	0.37 x 0.37 0.74 x 0.12	17 x 193 9 x 199	2 345 000 2 345 000	40 000 40 000

Table 1: Main parameters of the PIV recordings from the different experiments.

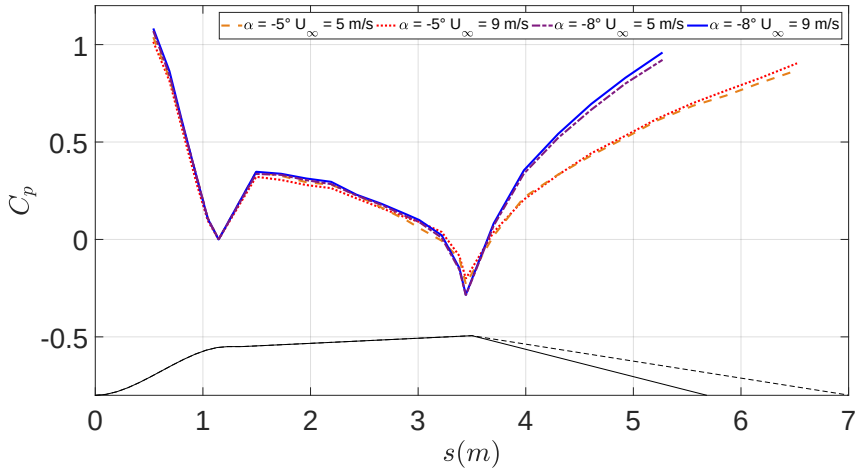

Figure 6: Evolution of the pressure coefficient C_p along the two ramp angles and for the two inlet velocities, s is the curvilinear coordinates along the ramp surface.

creating a localized adverse pressure gradient (APG) immediately after this section. This APG region leads to a sudden increase in both C_p and $\frac{dC_p}{ds}$ values. The flow then accelerates further in the favorable pressure gradient (FPG) region, which causes C_p to continue decreasing until it reaches another suction dip near the transition point between the FPG and APG regions. Around this transition, the pressure gradient rises sharply before gradually decreasing, remaining positive across the entire APG region. In the APG section, the flow decelerates, resulting in a gradual increase in the pressure coefficient.

For both the $\alpha = -5°$ and $\alpha = -8°$ plates a similar pressure coefficient is observed up to the transition from the FPG to the APG region. Then,

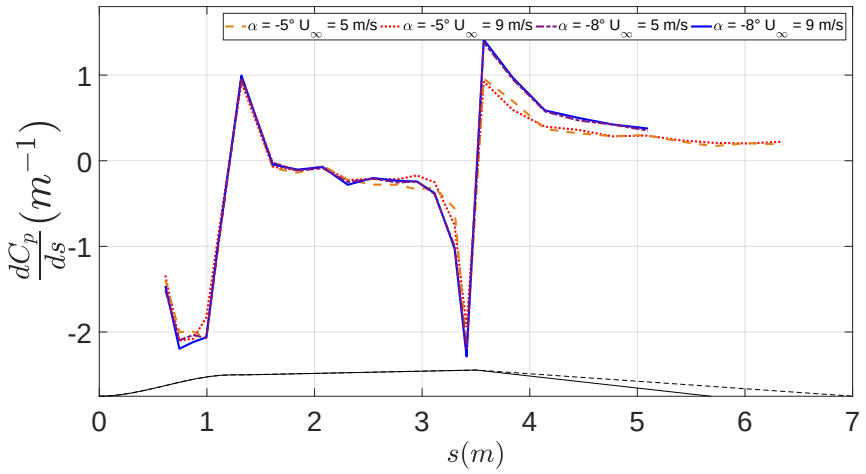

Figure 7: Evolution of the streamwise derivative of the pressure coefficient $\frac{dC_p}{ds}$ along the two ramp angles and for the two inlet velocities, s is the curvilinear coordinate.

around the articulation region (beginning of the APG flat plate, $x = 0$), the $-8°$ APG configuration has a stronger suction peak and accordingly, a higher jump in the pressure gradient. This supports the assumption that both experiments have a similar flow history leading up to the APG ramps and therefore the differences observed will only be due to the pressure gradient or a Reynolds number effect. Moreover, in the APG region a nearly constant pressure gradient is achieved as expected using the ramps.

3.2. Skin friction and friction velocity

To determine the friction velocity in the case of a wall-bounded flow, the most wildly use technique is the Clauser chart method proposed by Clauser (1954). This approach relies on the existence of a logarithmic layer near the wall. Therefore, by plotting in inner variables $U^+ = \frac{U}{u_\tau}$ as a function of $y^+ = \frac{yu_\tau}{\nu}$ in a semi-logarithmic scale (with the x-axis being the one in a logarithmic scale), the overlap region of the boundary layer is a straight line (Fig. 9). The following equation gives this line that is known as the log-law:

$$u^+ = \frac{1}{\kappa} ln\ y^+ + C \tag{2}$$

where κ is the von Kármán constant and C is an additive constant. For ZPG boundary-layers, we usually have $\kappa = 0.41$ and $C = 5$. The value of κ is still

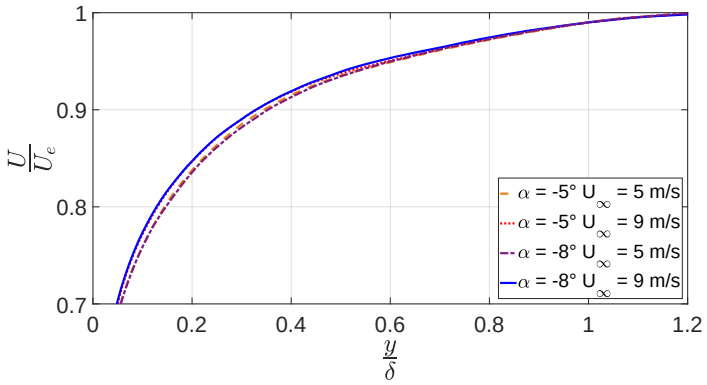

(a)

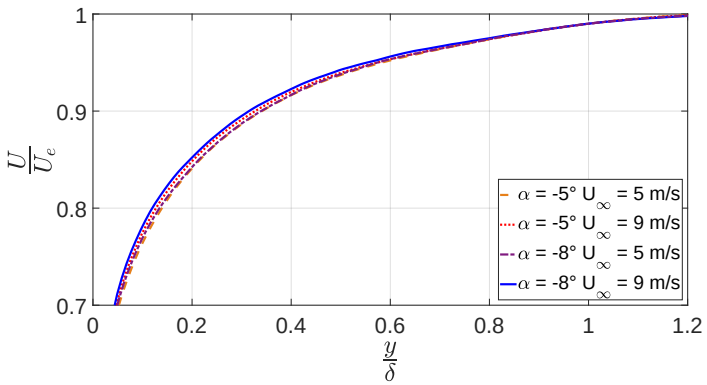

(b)

Figure 8: Profile comparison of the streamwise mean velocity at (a) $s = 3.0\,\mathrm{m}$ (at $x = -0.3\,\mathrm{m}$) and (b) $s = 3.1\,\mathrm{m}$ (at $x = -0.2\,\mathrm{m}$) with $x = 0$ the beginning of the APG region.

a subject of debate. In the present paper, we used 0.41 to agree with Cuvier et al. (2017). Fig. 9 (a) and (b) show the mean streamline velocity profile for the $\alpha = -5°$ and $\alpha = -8°$ plate, respectively, for a free-stream velocity of $U_\infty = 5$ m/s and compared to the log law given in Eq. (2). By assuming that κ, C and ν are constants, a least squared fit to the data obtained by the large PIV field was used to obtain the value of u_τ. This Clauser chart method allows an estimation of u_τ along the plate. Fig. 9 (a) and (b) show that the friction velocity in the wake region of the TBL increases from maximum of about 35 to about 50 at the extremity of the plate for increasing angle and thus, for a stronger APG.

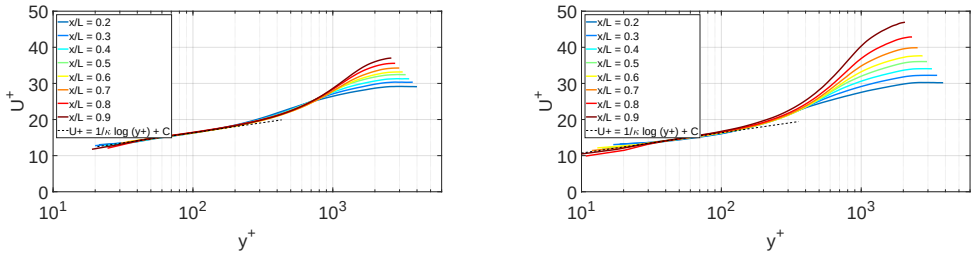

Figure 9: profiles of streamwise velocity along the ramp for $U_\infty = 5$ m/s a) $\alpha = -5°$ and b) $\alpha = -8°$ in inner representation $U^+ = f(y^+)$.

Even though the existence of a logarithmic region in APG flows remains a subject of ongoing debate, Monty et al. (2011) have shown that for a mild pressure gradient, the Clauser chart method is still suitable, but needs to be used with caution in strong pressure gradient conditions, as it can result in highly inaccurate values for u_τ, especially when the flow nears separation.

As seen in Fig. 9, we assume that a logarithmic layer can be used to determine u_τ by the Clauser chart method in the present contribution especially since we are far from the separation.

For both datasets, this method was used on the data from the large field 2D 2C PIV set. To assess the quality of this method, we use the near-wall direct measurement of u_τ at the 3 stations previously detailed and compare them to the value obtained using the data from the large field of view and the Clauser chart method. For the EuHIT experiment, the friction velocity at the stations was determined using Time-Resolved High Magnification PIV (TRHM-PIV), employing a wall-shear rate measurement technique introduced by Willert (2015). This method extracts highly spatially resolved time series velocity to estimate both the unsteady and mean wall-shear strain rate. Specifically, it uses a one-dimensional cross-correlation approach, where rows of pixels located at the same wall-normal distance but separated by a few time steps are analysed. A one-dimensional Gaussian peak is then fitted at the point of maximum correlation to obtain subpixel accurate displacement information for the given row. By combining this displacement with the magnification factor M and the time interval Δt, an estimate of the streamwise velocity at a given wall distance is derived. For the ONERA experiment, a variant of this method is used which consists at analyzing the images by using rectangular windows with the small dimension in the wall

normal direction to capture the mean gradient with high spatial resolution. The unsteady velocity estimates are averaged over the full sequence length to produce a mean streamwise velocity for each wall-normal position. Finally, the average wall shear strain rate is calculated by fitting a least squares line to the linear portion of the data, yielding an estimate of the wall shear stress, which is proportional to the friction velocity.

To compare the results of theses two methods, we compare the values of $C_f = 2\frac{u_\tau^2}{U_e^2}$ as shown in Fig. 10. The figure indicates that while there are some discrepancies between the C_f values obtained using the Clauser chart method and those derived from with TRHM-PIV, these differences are relatively small. The uncertainty of u_τ by the direct measurement is estimated to be better than 1% with a confidence interval of 95%. This uncertainty is estimated mainly by the convergence error of the mean profile and the derivative (see Foucaut and Stanislas, 2002). The uncertainty by Clauser chart is more difficult to evaluate and is assumed to be of the order of 2%. This uncertainty contains a random part which is probably small linked to the convergence error and a bias due to the method and the model used. Thin lines plotted in Fig. 10 for the two cases at 9 m/s represent a $\pm 5\%$ bound on C_f corresponding to about 2% on u_τ and 0.5% on U_e. They show that the estimation of u_τ by the Clauser chart is in the good range of uncertainties. Only for the angle of $-8°$ the Clauser chart method underestimates slightly the value of C_f and thus, of u_τ for the last station corresponding $x/L = 0.82$. In Fig. 10 this underestimation seems to appear for $x/L > 0.6$ and is probably linked to pressure gradient which may be begin to be too strong (Monty et al., 2011).

This minor variance suggests that the Clauser chart method, despite its theoretical limitations still provides results that are reasonably consistent with those obtained from the direct TRHM-PIV approach. Specifically, for mild to moderate adverse pressure gradients, the Clauser chart method remains a viable and effective tool for estimating the friction velocity, even though caution is advised for more severe pressure gradients where deviations might become more pronounced.

The measured values of u_τ provide the evolution of the friction Reynolds number $Re_\tau = \frac{\delta u_\tau}{\nu}$ shown in Fig. 11. The Reynolds number seems relatively constant along the ramps, particularly between $x/L > 0.1$ and $x/L > 0.6$. A slight decrease can be observed for $\alpha = -8°$ when $x/L > 0.6$ which is probably linked to the uncertainty of u_τ for this angle. The difference of

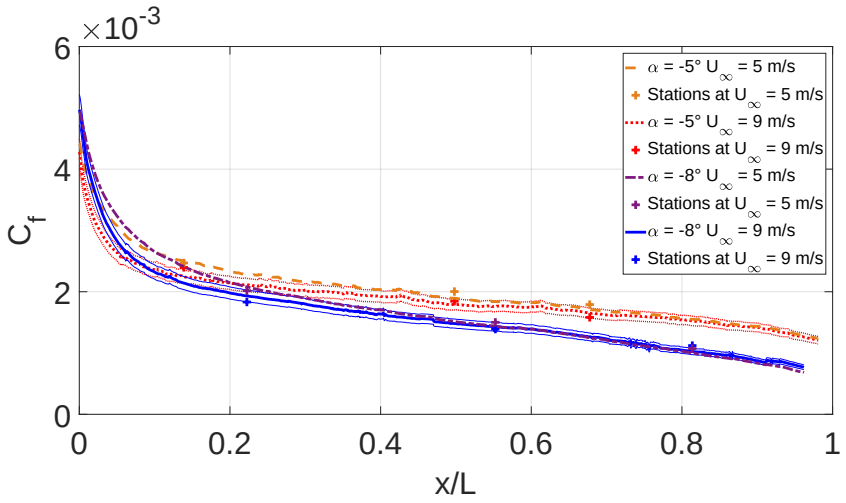

Figure 10: Comparison of C_f values calculated using the logarithmic law (lines) and the direct measurement (dots) of the friction velocities at the stations near wall for $\alpha = -5°$ and $\alpha = -8°$ and for the two inlet velocities.

Reynolds number between the two angles are relatively small for the same inlet velocity and are of the order of 2100 and 3500 for $U_\infty = 5$ m/s and $U_\infty = 9$ m/s, respectively. The uncertainty of this Reynolds number is relatively high, estimated at about 5% (see error bars) because both δ and u_τ are difficult to measure. Nevertheless, it is interesting to observe that along the ramp δ increases while u_τ proportionally decreases, since their product and thus, Re_τ is fairly constant within its range of uncertainty. This suggests that this APG TBL is nearly in equilibrium, which is subsequently explored.

3.3. Equilibrium of the adverse pressure gradient turbulent boundary layer

The study of turbulent flows is challenging due to the complex, non-linear, and multi-scale nature of the flow phenomena. To simplify this complexity, the concept of an "equilibrium turbulent layer" was introduced by Clauser (1954). An equilibrium layer is characterized by the slow variation of non-dimensional parameters, such as the shape factor H or skin friction coefficient C_f, with distance from the origin. The self-preserving nature of the outer regions allows for the adoption of reasonable assumptions that significantly simplify the analysis. Clauser (1954) thus defined the non-dimensional pres-

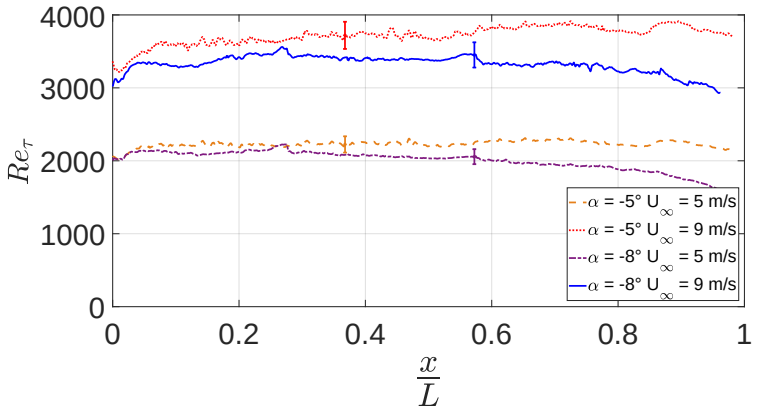

Figure 11: Evolution of the Reynolds number Re_τ versus the position along the ramp $\frac{x}{L}$

sure gradient parameter:

$$\beta = \frac{\delta^*}{\rho u_\tau^2}\frac{\partial P}{\partial x} \tag{3}$$

For equilibrium boundary layers, β remains constant, and Clauser (1954) expected that such layers exhibit dynamic similarity at all positions in both mean and fluctuating velocity fields. A specific case of this is the zero pressure gradient (ZPG) boundary layer, which aligns with Clauser's definition of equilibrium as $\frac{dP}{dx} = 0$ and therefore $\beta = 0$. Fig. 12 shows the evolution of the Clauser pressure gradient parameter β along the ramps in the APG region. In the case of the $-8°$ plate, we can observe that β is not constant and only stabilizes at a value of about 3.5 for a small region of the ramp between $x/L = 0.1$ and 0.4. This could indicate that the flow is not fully at equilibrium and therefore, the mean velocity cannot be scaled properly. Nevertheless, the increases of β can be amplified by the underestimation of u_τ discussed previously. In contrast, the value of β for the $-5°$ plate seem to be relatively constant with a value between 2 and 3 between $x/L = 0.05$ and 0.75 m suggesting that the flow over the $-5°$ ramp is in equilibrium. Clauser (1954) gives another evaluation of the equilibrium based on the plot $\frac{\Delta}{\delta} = f(G)$ where $\Delta = \int_0^\infty \frac{U_e - U(y)}{u_\tau}\, dy = \delta^* U_e/u_\tau$ and G is an integral parameter:

$$G = \int_0^\infty \left(\frac{U_e - U(y)}{u_\tau}\right)^2 d(\frac{y}{\Delta}) \tag{4}$$

Figure 13 shows this evolution for the two angles and the two inlet veloci-

ties. It is clear that G shows the same linear evolution for both the velocities but the slopes are different depending on the angle. The slope are 0.6 and 0.65 for $-8°$ and $-5°$, respectively. The linear behavior is obtain for G larger than 10 and 8 for $-8°$ and $-5°$, respectively. These two values are obtained at $x/L \approx 0.15$. The three points are the parameters studied by Clauser (1954). The linear evolution of $\frac{\Delta}{\delta} = f(G)$ could demonstrate a sort of equilibrium. In Fig. 13, the points correspond to the study of Clauser (1954) presented in Fig. 12 of his paper.

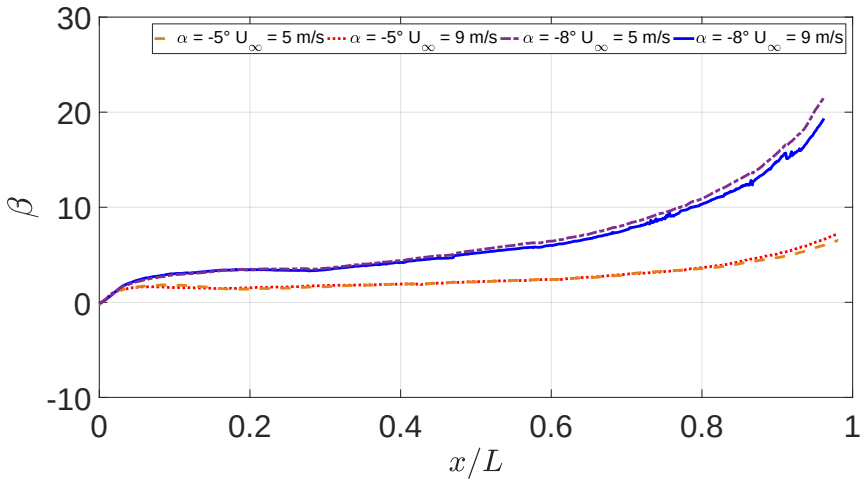

Figure 12: Evolution of the Clauser parameter β as a function of the ordinate normalized by the length of the ramp x/L.

Another pressure gradient parameter to determine if the flow is at equilibrium was suggested by George and Castillo (1997):

$$\Lambda \equiv \frac{\delta}{\rho U_e^2 \frac{d\delta}{dx}} \frac{dP_e}{dx} \sim \text{constant}, \tag{5}$$

with George and Castillo (1997) defining the conditions for equilibrium as:

$$\frac{d\delta}{dx} \sim \frac{\delta}{U_e} \frac{dU_e}{dx} \tag{6}$$

Because at equilibrium Λ is a constant the integration of Eq. (6) yields:

$$U_e \sim \delta^{-\Lambda} \tag{7}$$

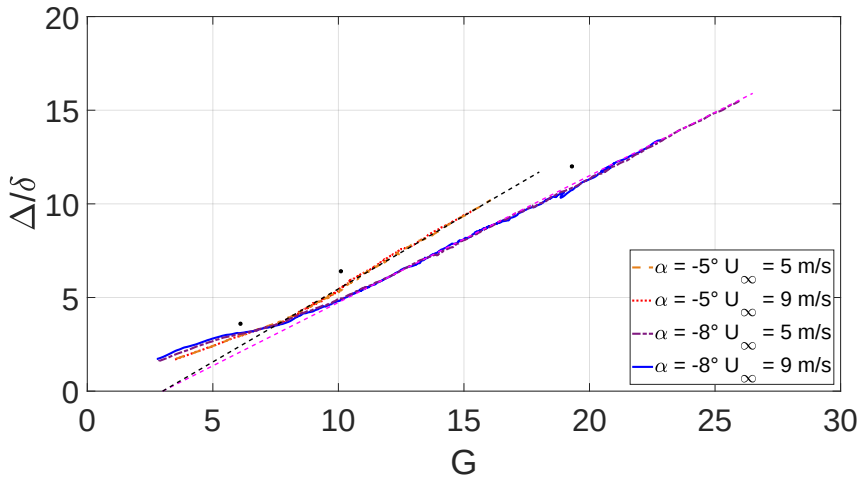

Figure 13: Relationship $\Delta/\delta = f(G)$ for equilibrium turbulent velocity profile following Clauser (1954).

To obtain Λ we plot U_e as a function of δ in a log-log plot and then fit the slope which yields an estimate for $-\Lambda$. A spline least square interpolation improves the result of the fit. Fig. 14 shows that the pressure gradient parameter Λ is not constant over the entirety of the plates. For both cases, the pressure gradient parameter becomes constant starting from $x/L = 0.1$. Based on this criterion the flow can be considered to be at equilibrium from $x/L \approx 0.1$ to the end of the plate.

In conclusion, the criteria of Clauser (1954) and of George and Castillo (1997) show that the flow reaches an equilibrium from $x/L \approx 0.1$. This equilibrium is maintained up to $x/L \approx 0.8$ and 0.5 for $\alpha = -5°$ and $-8°$, respectively following Clauser's criterion but with an uncertainty due to the measurement of u_τ in the case of $-8°$. The criterion of George and Castillo (1997), which does not depend on u_τ, shows that the equilibrium extends to the end of the plate.

3.4. Shape factor H

The shape factor H is defined by the ratio of displacement and momentum thickness:

$$H = \frac{\delta^*}{\theta} \tag{8}$$

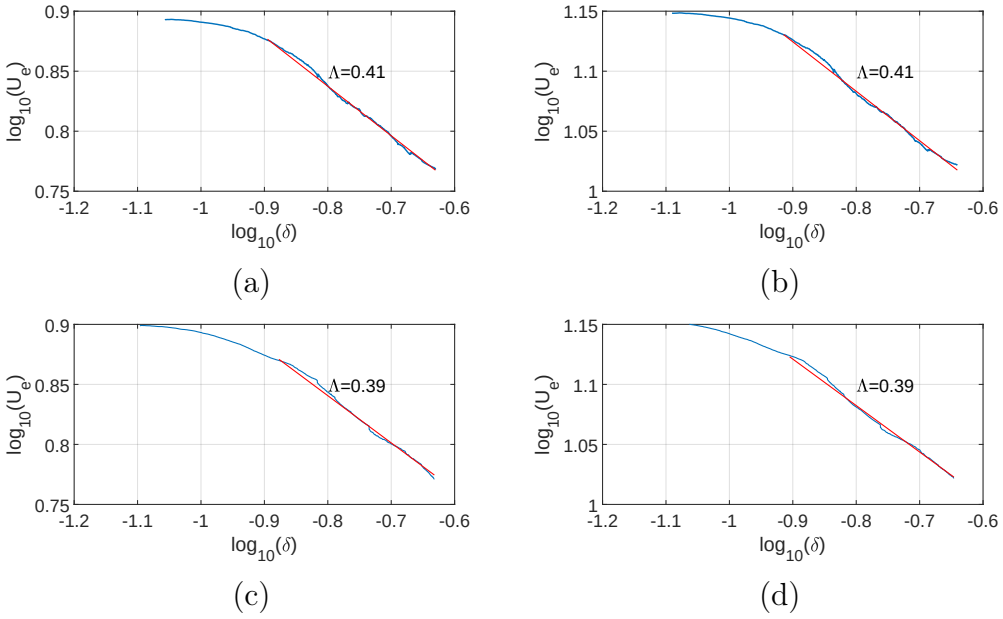

Figure 14: Pressure gradient parameter Λ for $\alpha = -5°$ at $U_\infty = 5$ m/s (a) and $U_\infty = 9$ m/s (b) and for $\alpha = -8°$ at $U_\infty = 5$ m/s (c) and $U_\infty = 9$ m/s (d). The red line hows the region exhibiting the equilibrium range (Λ = constant).

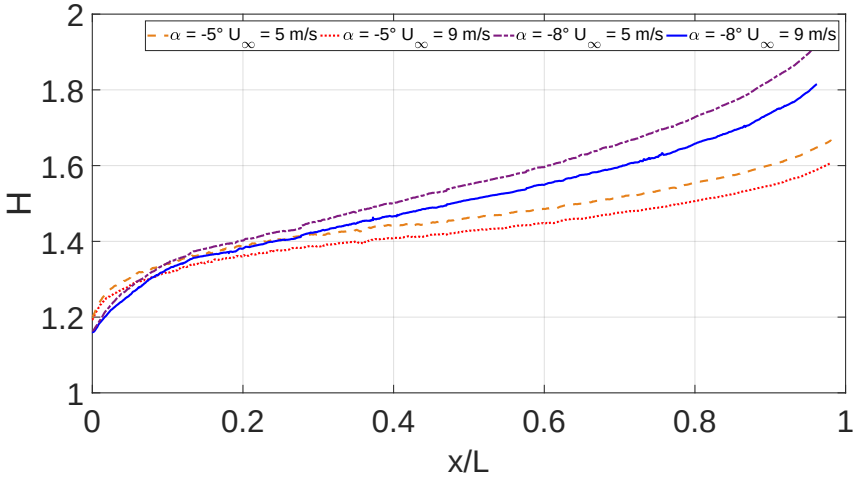

Figure 15: Evolution of the shape factor along the ramp for the two angles and the two inlet velocities.

Fig. 15 shows the evolution of the shape factor across the ramps. At the beginning of the plate, close to the corner between the FPG region and the APG region, we can observe significant changes in the value of the shape factor meaning that the variations of the pressure gradient that could be observed in Fig. 6 at the corner strongly impacts the near wall region. Moreover, the shape factor along the ramp indicates that for both cases, the boundary layer is far from separation as the expected value for flow separation would be 2.7 according to the literature. In addition, we can observe that for the same pressure gradient, the behaviour of the boundary layer thickness is very similar for both Reynolds numbers in this region.

3.5. Influence of the pressure gradient on the momentum thickness

The previous study of the shape factor showed that the behaviour of the boundary layer seemed to be heavily influenced by the pressure gradient rather than the Reynolds number. In this part we will focus on the influence of the pressure gradient on the momentum thickness to understand the influence the pressure gradient can have on the shape factor. We first start by comparing the order of magnitude in the von Kármán momentum integral equation in Fig. 16 :

$$\frac{u_\tau^2}{U_e^2} = \frac{\partial \theta}{\partial x} - \frac{\theta}{\rho U_e^2}(H+2)\frac{\partial P}{\partial x} \tag{9}$$

We can observe that $\frac{u_\tau^2}{U_e^2}$ is smaller than the two other terms and $\frac{\partial \theta}{\partial x}$ is of the same order of magnitude than $\frac{\theta}{\rho U_e^2}(H+2)\frac{\partial P}{\partial x}$.

We can rewrite Eq. (9) as follows:

$$\frac{\partial \theta}{\partial x} = \frac{C_f}{2}(1 + \frac{H+2}{H}\beta) \tag{10}$$

If we assume that $\frac{H+2}{H}\beta >> 1$ then we could write :

$$\frac{\partial \theta}{\partial x} = \frac{\theta}{L_p} \tag{11}$$

where $L_p = \frac{\rho U_e^2}{\frac{\partial P}{\partial x}(H+2)}$. If L_p is independent of x the integration of Eq. (11) is trivial and gives an exponential evolution for θ.

The evolution of $\frac{L_p}{L}$ is shown on Fig. 17 as a function of $\frac{x}{Hr}$ with L the length of the ramp and $Hr = 0.306\,\mathrm{m}$ the maximum high of the ramp at

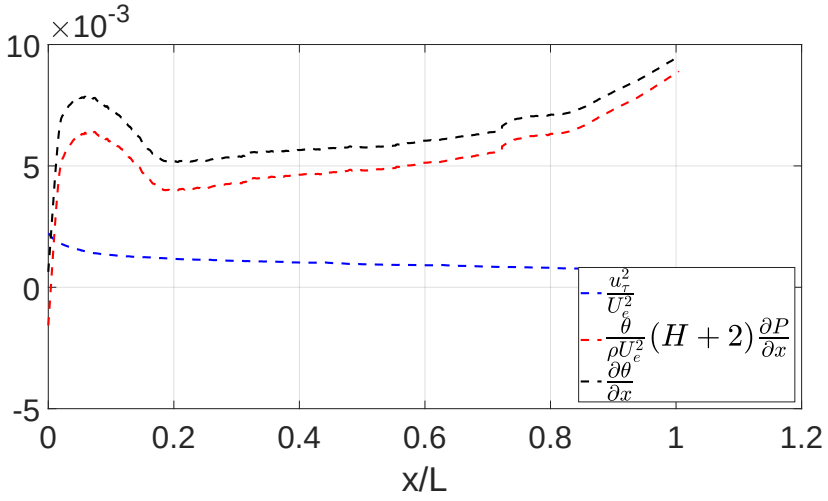

Figure 16: Comparison of the terms of the von Kármán momentum integral equation for the $\alpha = -5°$ ramp at $U_\infty = 5$ m/s.

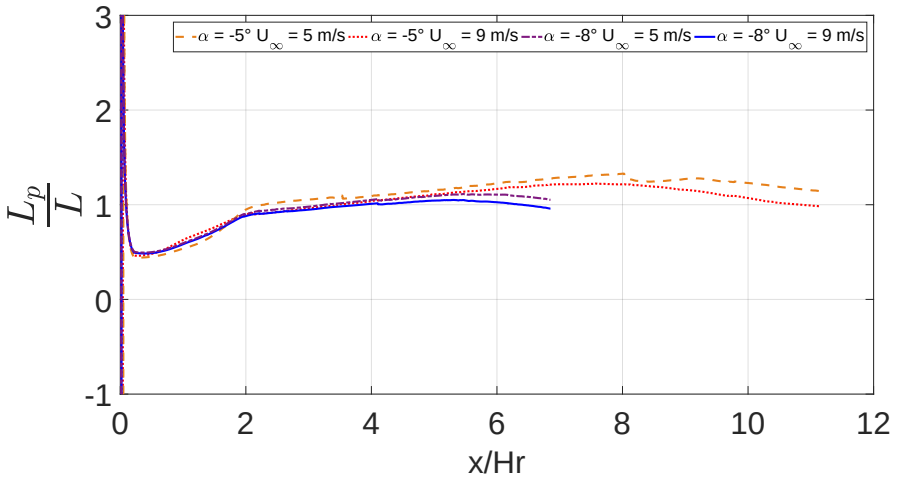

Figure 17: Evolution of $\frac{L_p}{L}$ along the ramp for the two angles and the two inlet velocities.

$x = 0$. The values of $\frac{L_p}{L}$ look similar for all experiments and seem relatively constant approximately equal to 1 for $\frac{x}{Hr}$ greater than about 2.

In our case we cannot simplify Eq. (10) and we have to integrate Eq. (9)

by assuming $\frac{u_\tau^2}{U_e^2}$ is independent of x.

$$\theta = -\frac{u_\tau^2}{U_e^2} L_p + K e^{\frac{x}{L_p}} \tag{12}$$

The parameter L_p is taken as its average along the plate between the minimum around $\frac{x}{Hr} = 0.7$ and the end of the plate $x = L$. We optimise the value of the parameter K and the result of the model is shown on Fig. 18.

In this figure, θ, normalized by the maximum height of the ramp Hr, is plotted as a function of $\frac{x}{L}$. We can then observe that this scaling seems to be only slightly sensitive to the velocity and thus to the Reynolds number with the pressure gradient appearing to have no influence. As the model given by Eq. (12) does not depend on the pressure gradient, it is only shown for each velocity at a single angle, to avoid overloading the figure.

We can then see that this model offers a good estimate of the momentum thickness, even at the beginning of the plate where the flow is affected by the corner between the FPG region and the APG region and where it should not work. The value of the parameters can be found in Table 2. The optimization seems to yield reasonable values and the ratio $\frac{L_p}{L}$ is close to 1. This comparison seems to validate the results of the optimization and therefore the estimated value of K that appears to be relatively constant in our model with a mean value around 0.013.

Slope	$\alpha = -5°$	$\alpha = -5°$	$\alpha = -8°$	$\alpha = -8°$
U_∞	5 m/s	9 m/s	5 m/s	9 m/s
K	0.0153	0.0136	0.013	0.0117
L_p	3.84	3.62	2.08	1.99
L_p/L	1.1	1.04	0.95	0.91

Table 2: Results of optimisation

Fig. 19 shows the evolution of the Reynolds number Re_θ based on the momentum thickness and the external velocity U_e. Along x/L no observable difference due to Reynolds number for the two ramp angles is found and thus, for the two pressure gradient ranges. This result is interesting because it suggests that the effects of Reynolds number and the pressure gradient are decoupled and can be investigated separately.

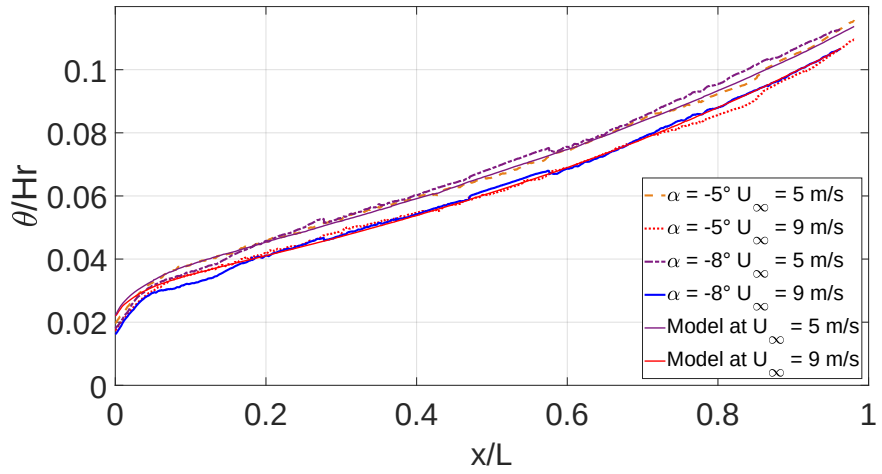

Figure 18: Momentum thickness θ **normalized by the maximum high of the ramp** Hr versus the position along the ramp $\frac{x}{L}$.

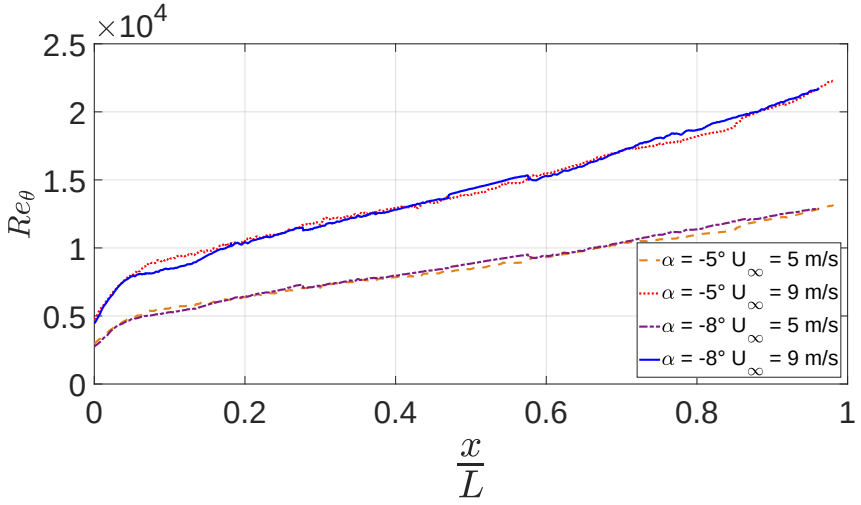

Figure 19: Evolution of the Reynolds number Re_θ versus the position along the ramp $\frac{x}{L}$.

4. Analysis

Developing a universal scaling approach for adverse pressure gradient boundary layers would provide significant advantages, allowing for the generalization of experimental findings across different setups and flow conditions.

A universal scaling would also facilitate the integration of diverse datasets, enabling a deeper understanding of the complex interactions within APG boundary layers and advancing our capacity to model and predict flow separation, drag, and other critical aerodynamic phenomena.

Following Clauser (1956), George and Castillo (1997), Zagarola and Smits (1998) and Pirozzoli and Smits (2023), we assume that there is a universal function F such as:

$$\frac{U_e - U(y)}{u_0} = F(\frac{y}{\delta_0}) \tag{13}$$

where $U(y)$ is the mean velocity profile as a function of the wall distance y, U_e is the velocity outside the boundary layer and u_0 and δ_0 are appropriate velocity and length scaling parameters, respectively, which are yet to be determined.

According to Pirozzoli and Smits (2023) we then have the following relationships:

$$U_e\delta^* = u_0\delta_0\chi \tag{14}$$

where δ^* is the displacement thickness of the boundary layer and

$$\chi = \int_0^\infty F(\frac{y}{\delta_0})\, d(\frac{y}{\delta_0}).$$

$$U_e\theta = u_0\delta_0(\chi - \frac{u_0}{U_e}\psi) \tag{15}$$

where θ is the momentum thickness and $\psi = \int_0^\infty F^2(\frac{y}{\delta_0})\, d(\frac{y}{\delta_0})$

Finally, combining these relationships yields:

$$H = \frac{\delta^*}{\theta} = \frac{\chi}{\chi - \frac{u_0}{U_e}\psi} \tag{16}$$

and we can obtain:

$$\frac{\psi}{\chi} = \frac{H-1}{H}\,\frac{U_e}{u_0} \tag{17}$$

Then, Eq. (17) allows the computation of $u_o = U_e\frac{H-1}{H}\frac{\chi}{\psi}$ and Eq. (14) gives the relationship between the scaling parameters u_0 and δ_0 such that $\delta_o = \delta^*\frac{H}{H-1}\frac{\psi}{\chi}$.

For a universal scaling, χ and ψ are constants and therefore we can enforce arbitrarily their values to be 1 (Pirozzoli and Smits, 2023). The resulting scaling parameters are then $u_n = U_e\frac{H-1}{H}\frac{\chi}{\psi}$ and $\delta_n = \delta^*\frac{H}{H-1}\frac{\psi}{\chi}$. This scaling is valid for a zero pressure gradient TBL (Pirozzoli and Smits, 2023),

following its derivation there is no reason that it is not in the case of an APG TBL. Maciel et al. (2018) propose a theory based on the same development. However they include the value of the velocity at $\delta/2$ in the scaling parameter which do not bring improvement as compare with the scaling of Pirozzoli and Smits (2023).

According to Coles (1956), as far as the turbulent characteristics are concerned, for the inner region of the ZPG TBL the scaling parameters are the friction velocity u_τ and the kinematic viscosity ν and for the outer region u_τ and the boundary layer thickness δ seems to be a good scaling set of parameters. In the presence of an APG, Romero et al. (2022) propose the inclusion of the pressure gradient in the velocity scale based on the near wall RANS equation:

$$\nu\frac{\partial U}{\partial y} - \overline{u'v'} = u_\tau^2 + \frac{y}{\rho}\frac{\partial P}{\partial x} \tag{18}$$

where $\overline{u'v'}$ is the Reynolds shear stress, ρ is the fluid density. As suggested by Romero et al. (2022), the velocity scale can be taken as $u_{hyb} = \sqrt{u_\tau^2 + \frac{y}{\rho}\frac{\partial P}{\partial x}}$. They used u_{hyb} with ν/u_τ as inner scaling parameter. To characterize the outer region, δ could be used as length scale coupled with u_{hyb}. This scaling is in agreement with Coles (1956) but does not present a χ constant. For this reason the new length scale $\delta_{hyb} = \frac{Ue\delta^*}{\sqrt{u_\tau^2+\frac{y}{\rho}\frac{\partial P}{\partial x}}}$ is proposed which satisfies Eq. (14). In the case of a zero pressure gradient the proposed scaling reduces to the one of Clauser (1956) with $\Delta = \frac{U_e}{u_\tau}\delta^*$ and u_τ.

Table 3 shows the different scaling parameters from the literature (George and Castillo, 1997; Clauser, 1956; Zagarola and Smits, 1998; Pirozzoli and Smits, 2023 and Romero et al., 2022), to which the proposed scaling will be compared. Table 3 gives also the expression of $\frac{\psi}{\chi}$ which should be constant following Pirozzoli and Smits (2023). Except the scaling of Romero et al. (2022), all scaling gives $\chi = 1$.

Fig. 20 shows the evolution of $\frac{\psi}{\chi}$ with x/L only for $U_\infty = 9$ m/s and $\alpha = -8°$ for each set of scaling parameters following Eq. (17). For the scaling of Romero et al. (2022) which varies with y the plot is done at $y = \delta/2$. Only the scaling of Pirozzoli and Smits (2023) is $\frac{\psi}{\chi}$ constant and equal to 1. For the other scaling this ratio increases with x. In the case of Clauser (1956), the ratio $\frac{\psi}{\chi}$ is equivalent to its parameter G with a value between 10 and 20 linearly increasing with x which is in agreement with the results presented in Fig. 13.

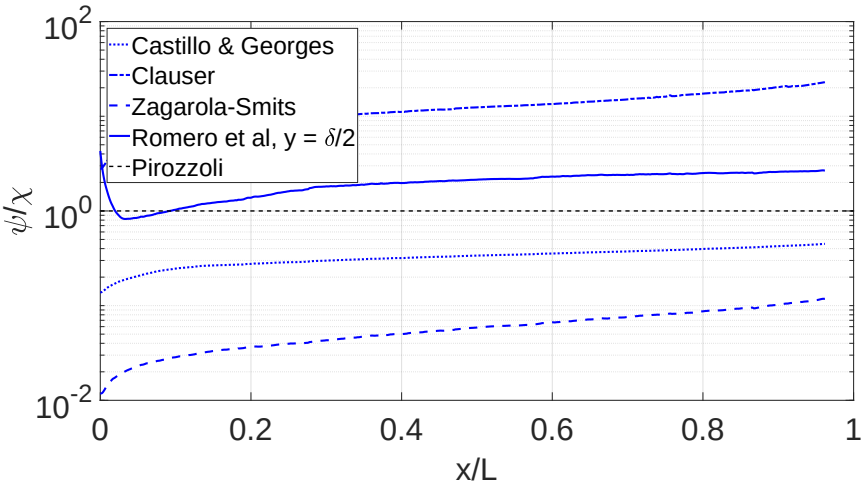

Figure 20: $\frac{\psi}{\chi}$ versus the position along the ramp $\frac{x}{L}$ for $U_\infty = 9$ m/s and $\alpha = -8°$.

To be able to use the scaling of Romero et al. (2022), we need to be mindful of the variations of $\frac{\partial P}{\partial x}$. The scaling velocity and length are quite sensitive to small variations of the pressure gradient due to random measurement error. To minimize the error, the value of the measured pressure coefficient is smoothed in the calculation of the pressure gradient.

For the last row of Table 3, the scaling length is a function of y. As a result, the calculation leading to Eq. (14) needs to be confirmed. Eq. (19) demonstrates that these conditions remain valid, particularly for higher values of $\frac{y}{\delta^*}\beta$:

$$U_e\delta^* = U_e\delta^* \int_0^\infty \frac{U_e - U}{u_0} \frac{1 + \frac{y}{\delta^*}\beta}{1 + \frac{3}{2}\frac{y}{\delta^*}\beta}\, d(\frac{y}{\delta_0}) \simeq \frac{2}{3} u_0 \delta_0 \chi \tag{19}$$

4.1. Mean velocity

Before comparing the datasets, we first analyze the different scaling parameters across the ramps to determine the most suitable scaling method. Fig. 21, 22, 23 and 24 compare the different scaling parameters of Table 3 respectively for the $-5°$ plate at $U_\infty = 5\,\mathrm{m/s}$ and 9 m/s and the $-8°$ plate at $U_\infty = 5\,\mathrm{m/s}$ and $9\,\mathrm{m/s}$. In this comparison, we focus on the flow relatively far from the beginning of the ramp to evaluation and eventual stabilization, based on the equilibrium analysis of the boundary layer. The comparison

	Scaling velocity	Scaling length	$\frac{\psi}{\chi}$
George and Castillo (1997)	U_e	δ^*	$\frac{H-1}{H}$
Clauser (1956)	u_τ	$\Delta = \frac{U_e}{u_\tau}\delta^*$	$\frac{H-1}{H}\frac{U_e}{u_\tau}$
Zagarola and Smits (1998)	$u_z = U_e\frac{\delta^*}{\delta}$	δ	$\frac{\delta^*-\theta}{\delta}$
Pirozzoli and Smits (2023)	$u_n = U_e\frac{H-1}{H}$	$\delta_n = \frac{H}{H-1}\delta^*$	1
Romero et al. (2022)	$u_{hyb} = \sqrt{u_\tau^2 + \frac{y}{\rho}\frac{\partial P}{\partial x}}$	δ	$\frac{H-1}{H}\frac{U_e}{\sqrt{u_\tau^2+\frac{y}{\rho}\frac{\partial P}{\partial x}}}$
Proposition	$u_{hyb} = \sqrt{u_\tau^2 + \frac{y}{\rho}\frac{\partial P}{\partial x}}$	$\delta_{hyb} = \frac{Ue\delta^*}{\sqrt{u_\tau^2+\frac{y}{\rho}\frac{\partial P}{\partial x}}}$	$\frac{H-1}{H}\frac{U_e}{\sqrt{u_\tau^2+\frac{y}{\rho}\frac{\partial P}{\partial x}}}$

Table 3: Different scaling parameters for TBL

starts at $x/L = 0.2$ m up to $x/L = 0.9$ m for the two plates, ensuring that the flow has reached a region of equilibrium.

From these results we observe that all the scaling parameters behave similarly. With increasing distance from the origin of the ramp up to about $x/L = 0.8$ the individual curves approach each other and then begin to diverge, probably because of increased variations of the pressure gradient near the changes in slope. The George and Castillo (1997) and Clauser (1956) scaling show one intersection of all the profiles. The Zagarola and Smits (1998) and Pirozzoli and Smits (2023) scaling show two intersections of all the profiles. The Romero et al. (2022) scaling does not show any intersection. This is probably due to the fact that χ is not constant. Nevertheless, it shows the same phenomenon of stabilization on the profiles. The proposed new scaling also shows an intersection which is more difficult to discern due to an improved collapse of the profiles in comparison to the previously introduced scalings.

In all cases, it is evident that no single scaling method is universally applicable across the entire ramp. However, the evolution of scaling across the ramps suggests that the further we move from the transition point at the start of the plate, the more effective the scaling becomes. To verify this hypothesis, we apply the scaling described by Pirozzoli and Smits (2023), using a constant ratio of $\frac{y}{\delta}$. We select a value of $\frac{y}{\delta} = \frac{1}{2}$ as this is where the

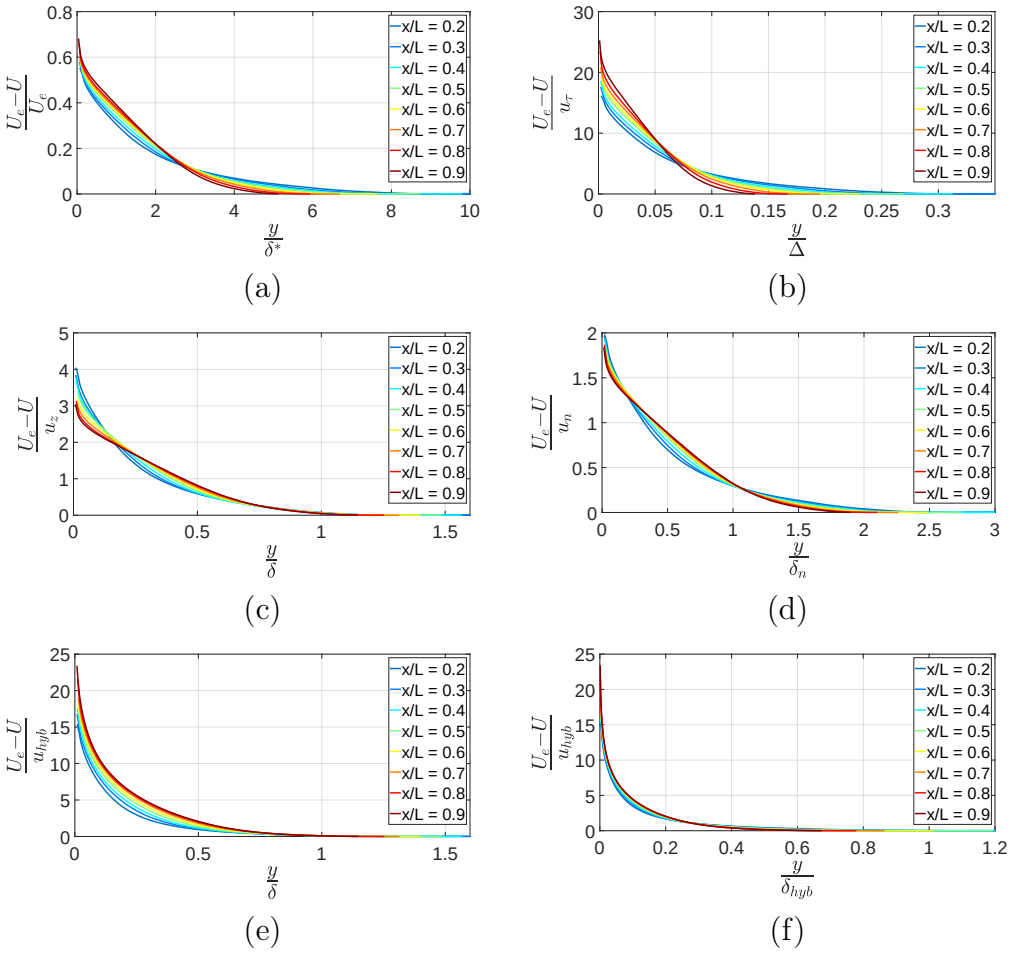

Figure 21: Comparison of mean velocity scaling along the $-5°$ ramp at 5 m/s. The scaling parameters are from George and Castillo (1997) (a) , Clauser (1956) (b), Zagarola and Smits (1998) (c), Pirozzoli and Smits (2023) (d), Romero et al. (2022) (e) and the present proposition (f).

largest differences are observed in the previous profiles in panel (d) of Figs. 21, 22, 23 and 24. Fig. 25 illustrates the evolution of this ratio across the ramps for all cases. For the $-5°$ plate, the mean velocity scaling stabilizes between $x/L = 0.65$ and 0.85, suggesting that the flow requires some distance along the ramp to stabilize before a universal scaling can be applied. Additionally, a perturbation near the end of the plate appears to disrupt the mean velocity scaling around $x/L = 0.85$ from the start of the plate. In contrast, for the $-8°$

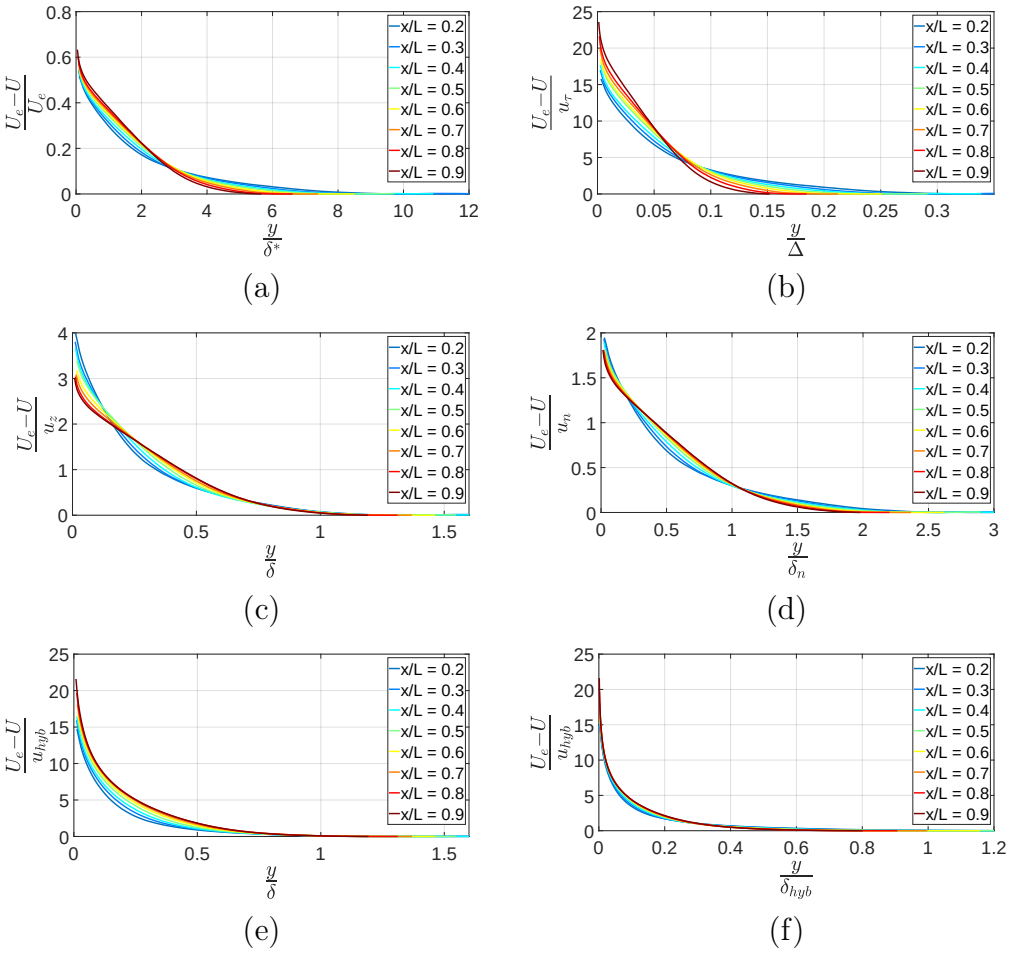

Figure 22: Comparison of mean velocity scaling along the $-5°$ ramp at 9 m/s. The scaling parameters are from George and Castillo (1997) (a), Clauser (1956) (b), Zagarola and Smits (1998) (c), Pirozzoli and Smits (2023) (d), Romero et al. (2022) (e) and the present proposition (f).

plate, the mean velocity scaling does not reach a constant value, although there is a slight plateau between $x/L = 0.7$ and 0.8, similar to the $-5°$ plate. This could indicate that the ramp used in the ONERA experiment was too short for the flow to fully stabilize, as the end of the plate also introduces disturbances. This suggests that while the flow may not fully stabilize across shorter ramps, the outer region is less sensitive to these effects. These observations support the hypothesis that, even in APG flows, universal

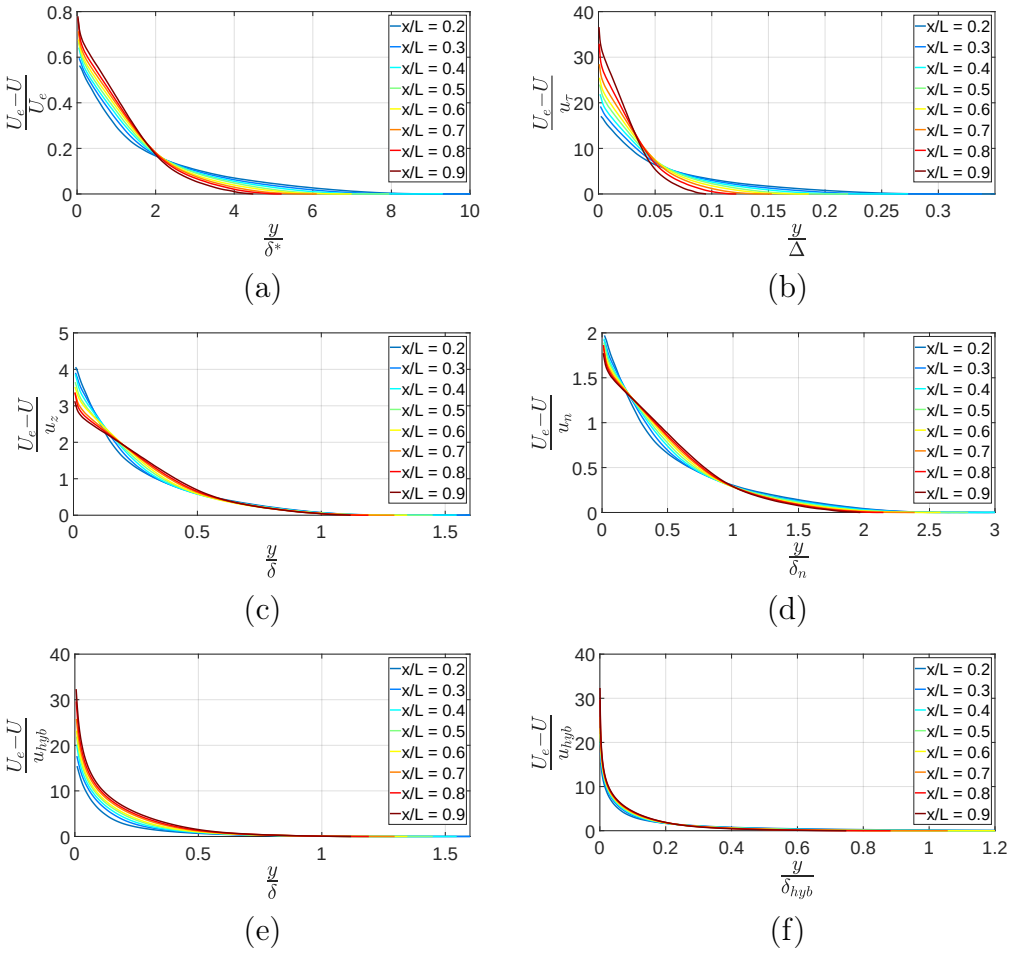

Figure 23: Comparison of mean velocity scaling along the $-8°$ ramp at 5 m/s. The scaling parameters are from George and Castillo (1997) (a) , Clauser (1956) (b), Zagarola and Smits (1998) (c), Pirozzoli and Smits (2023) (d), Romero et al. (2022) (e) and the present proposition (f).

scaling in the outer region can be achieved, similar to what is observed in zero pressure gradient (ZPG) flows.

To compare the two experiments, we will focus on the latter part of each plate, where the scaling appears to be most effective. We examine the scaling approaches introduced by Zagarola and Smits (1998), Pirozzoli and Smits (2023), Romero et al. (2022), and the present proposition, as these methods appear to be the most effective across the ramp. Fig. 26

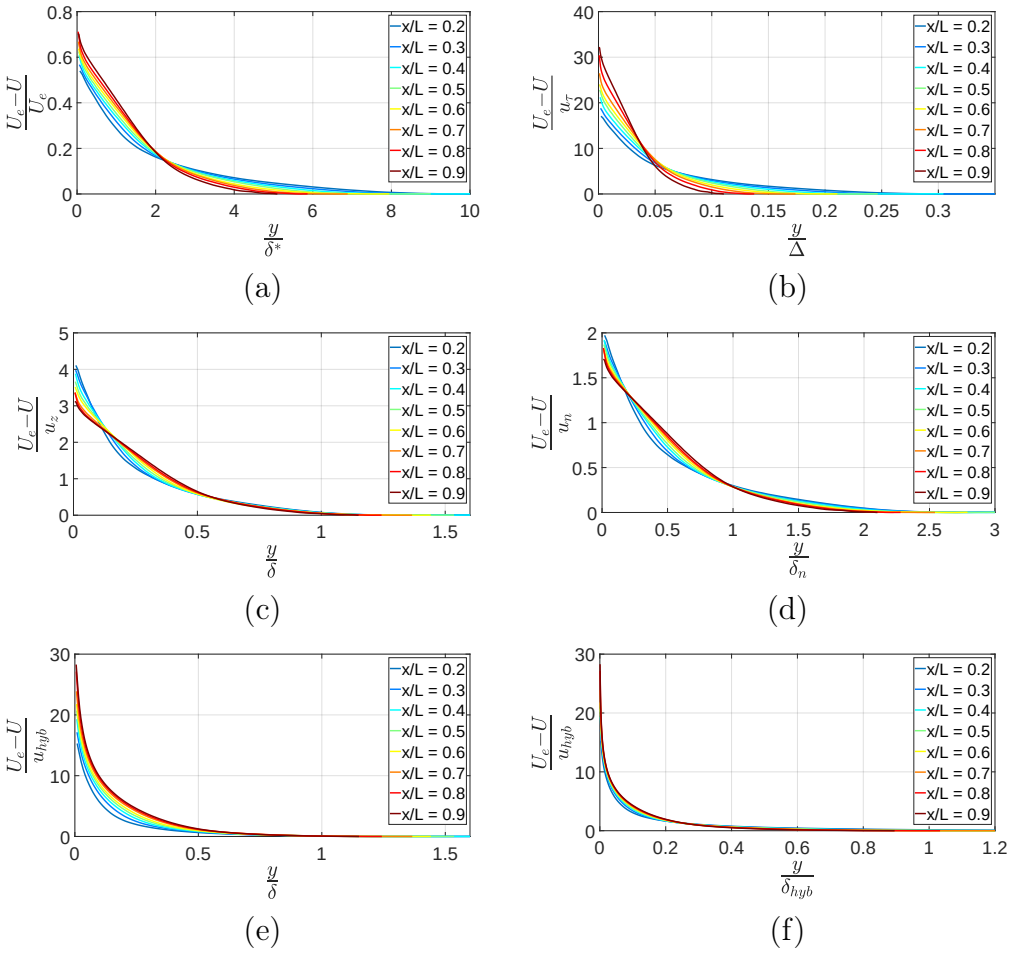

Figure 24: Comparison of mean velocity scaling along the $-8°$ ramp at 9 m/s. The scaling parameters are from George and Castillo (1997) (a) , Clauser (1956) (b), Zagarola and Smits (1998) (c), Pirozzoli and Smits (2023) (d), Romero et al. (2022) (e) and the present proposition (f).

compares these different mean velocity scaling methods for both pressure gradients obtained for the two angles and two Reynolds numbers obtained by the two inlet velocities as can be seen in Fig. 19. The various scaling parameters prove to be highly effective in the outer region, independent of both Reynolds number and pressure gradient. This suggests that, while universal scaling across the entire ramp remains elusive, the outer region of the boundary layer exhibits a degree of robustness to changes in flow

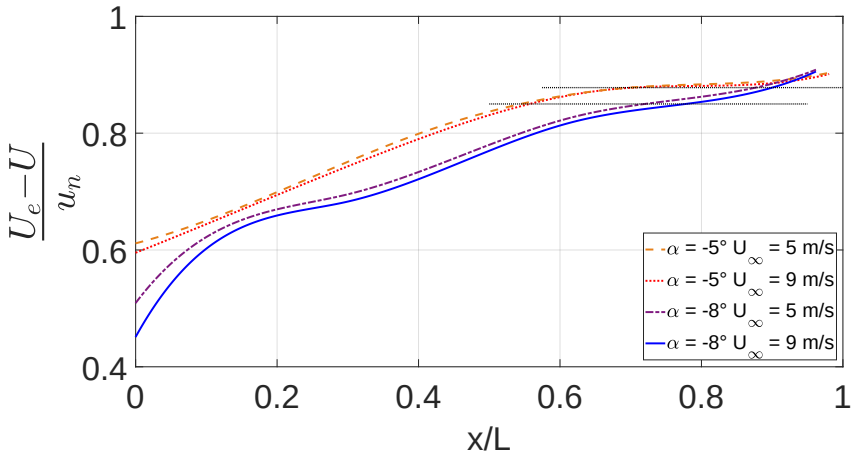

Figure 25: Pirozzoli scaling across the ramps at $\frac{y}{\delta} = \frac{1}{2}$.

conditions. Nevertheless the present proposition seems to give a very good set of scaling parameters for the cases proposed here. The similarity in behaviour across different Reynolds numbers and pressure gradients aligns with the self-preserving nature of the outer layers, as initially proposed by Clauser (1954) for equilibrium turbulent layers. In both, the $-5°$ and $-8°$ ramp cases, the scaling becomes more reliable as we move further downstream, indicating that once the boundary layer has had time to stabilize, the influence of upstream disturbances diminishes.

4.2. Reynolds stresses

The scaling of Reynolds stresses is crucial to understand the turbulent structure of the boundary layer, particularly in APG flows. Unlike mean velocity profiles, Reynolds stresses capture the fluctuating components of the flow, providing insights into turbulence intensity and momentum transport across the boundary layer. Effective scaling of these stresses allows for a unified representation across different flow conditions, helping to reduce the complexity introduced by variations in Reynolds number and pressure gradient. The intensification of large-scale structures due to the pressure gradient is well demonstrated in the work of Harun et al. (2013) and Sanmiguel Vila et al. (2017). Consequently, it plays an important role in Reynolds stress profiles. By applying consistent scaling methods, such as the scaling of Romero et al. (2022) which was designed for the Reynolds shear stress or our modified

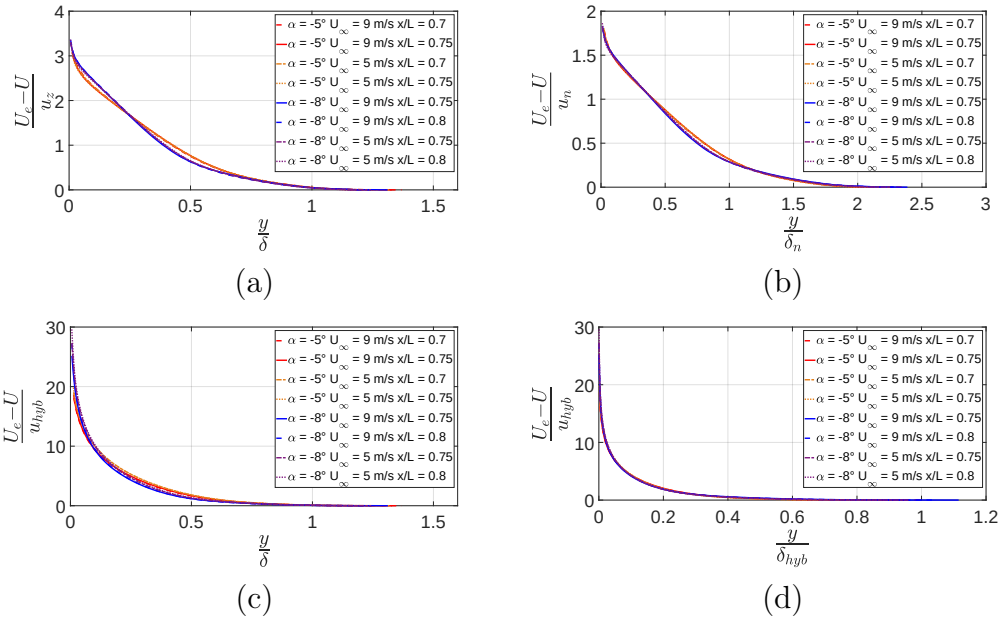

Figure 26: Comparison of mean velocity scaling for the two different Reynolds numbers and the two angles around $x/L = 0.75$. The scaling parameters are from Zagarola and Smits (1998) (a), Pirozzoli and Smits (2023) (b), Romero et al. (2022) (c) and the present proposition (d).

approach, we can more accurately compare turbulent behavior in diverse flow scenarios. Wei and Knopp (2023) propose a scaling based on the point of maximum Reynolds stress, showing good consistency in the non-equilibrium regime.

4.2.1. Inner scaling

First, Fig. 28 (a) and Fig. 28 (b) show the Reynolds shear stress along the ramp in inner scaling using u_τ and ν for the same inlet velocity $U_\infty = 5\,\mathrm{m/s}$ and thus, the same Reynolds number and for the two angles which create two different pressure gradients. The minimum value of these profiles increases with the position along the ramp due to the increase of the pressure gradient. As seen in Eq. (18), far from the wall the shear stress is given by

$$\overline{u'v'}^{+} = -1 - \frac{y}{\rho u_\tau^2}\frac{\partial P}{\partial x} = -1 - \beta\frac{y}{\delta *} = \frac{u_{hyb}^2}{u_\tau^2} \tag{20}$$

which is also plotted in dashed line in Fig. 28 (a) and (b) for the pressure gradient of $x/L = 0.9$. This profile is slightly under the corresponding PIV profile showing that the convection terms neglected close to the wall is not negligible. Following Romero et al. (2022), Fig. 28 (c) and (d) show the same Reynolds shear stress along the ramp but the velocity is normalized by u_{hyb} defined in Table 3 which take into account the pressure gradient effect in the scaling. Designed to be efficient in the inner region, this scaling normalizes the profiles very well for $y^+ < 300$ around $0.2 < x/L < 0.8$. Nevertheless, in Fig. 28 (c) and (d) we can observe more dispersion than for the mean velocity profiles in Fig. 9.

The dispersion can be due to a lack of convergence (the convergence error is of the order of 2% for the Reynolds stress) or to a filtering effect which varies along x given the fact that u_τ decreases while the structure scales increase along the ramp. To illustrate this last effect Fig. 27 shows a comparison of the Reynolds stress profiles obtained by low and high magnification experiments at the two furthest downstream stations for the same inlet velocity 5 m/s and the same angle $\alpha = -8°$. A slight filtering can be observed below $y^+ = 80$ which amounts to less than 4% of the boundary layer thickness and should not affect the results concerning the outer layer described in the following.

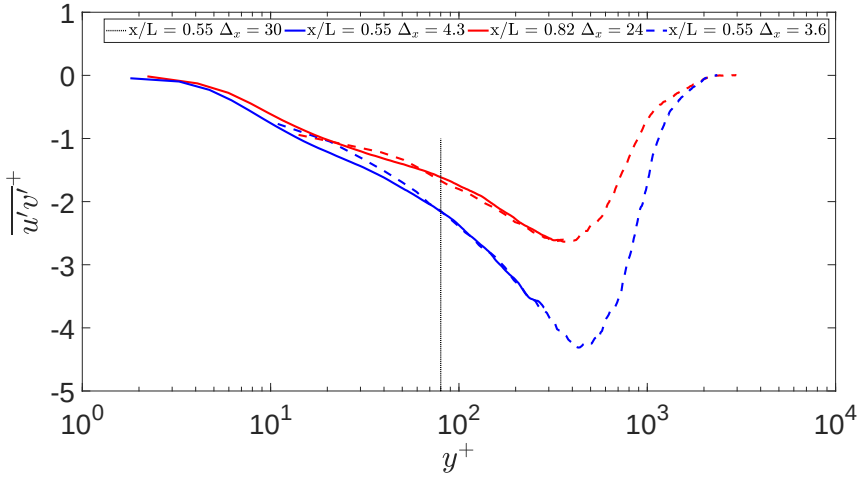

Figure 27: Profiles of Reynolds shear stress ($\overline{u'v'}$) at 5 m/s along the ramp at $\frac{x}{L} = 0.55$ and $\frac{x}{L} = 0.82$ obtained by low and high magnifications.

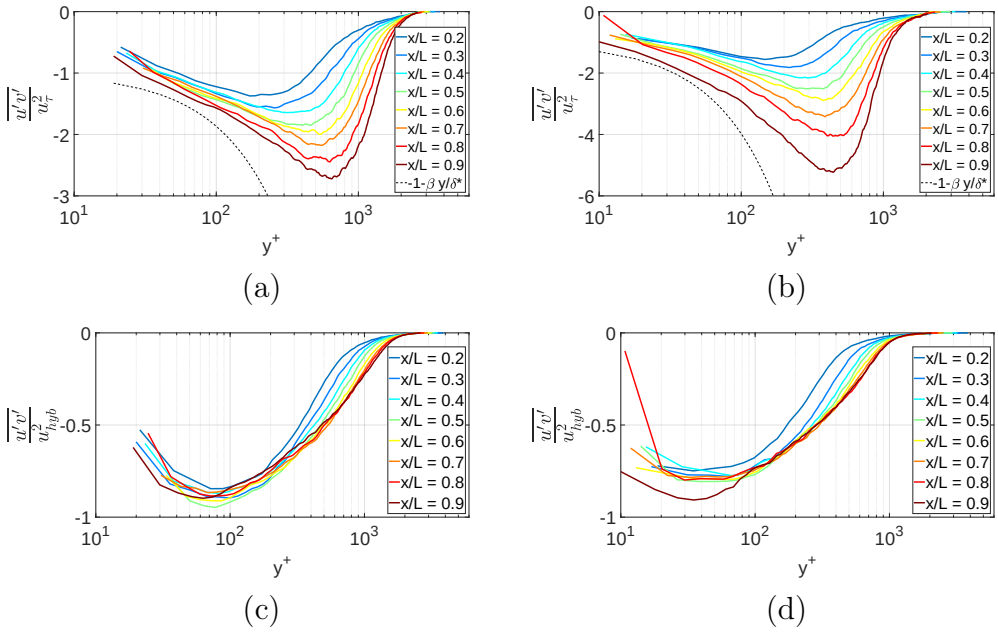

Figure 28: Profiles of Reynolds shear stress ($\overline{u'v'}$) along the ramp at 5 m/s. The scaling parameters are the inner one for $\alpha = -5°$ (a) and for $\alpha = -8°$ (b), and the one of Romero et al. (2022) for $\alpha = -5°$ (c) and for $\alpha = -8°$ (d).

4.2.2. Outer scaling

In addition to mean velocity profiles, the same outer scaling parameters as in Figs. 21, 22, 23 and 24 can be applied to the Reynolds stresses to examine their ability to capture turbulent fluctuations. This approach allows for a unified comparison of turbulence intensity across different Reynolds numbers and pressure gradients. Using consistent scaling across both the mean velocity and Reynolds stresses provides a comprehensive framework to study the turbulent structure in boundary layers, particularly in the context of adverse pressure gradients. Fig. 29 shows the evolution of the Reynolds shear stress scaled using the parameters of Table 3 on the $-5°$ plate at $U_\infty = 5$ m/s.

As expected, the scaling (i.e. Fig. 29 (e)) introduced by Romero et al. (2022), along with our new proposition (i.e. Fig. 29 (f)) that is heavily inspired by this work, proves to be the most effective for scaling the Reynolds shear stress. The scaling velocity u_{hyb} is based on balancing stress terms by combining the wall-shear-stress velocity with a pressure-stress-based veloc-

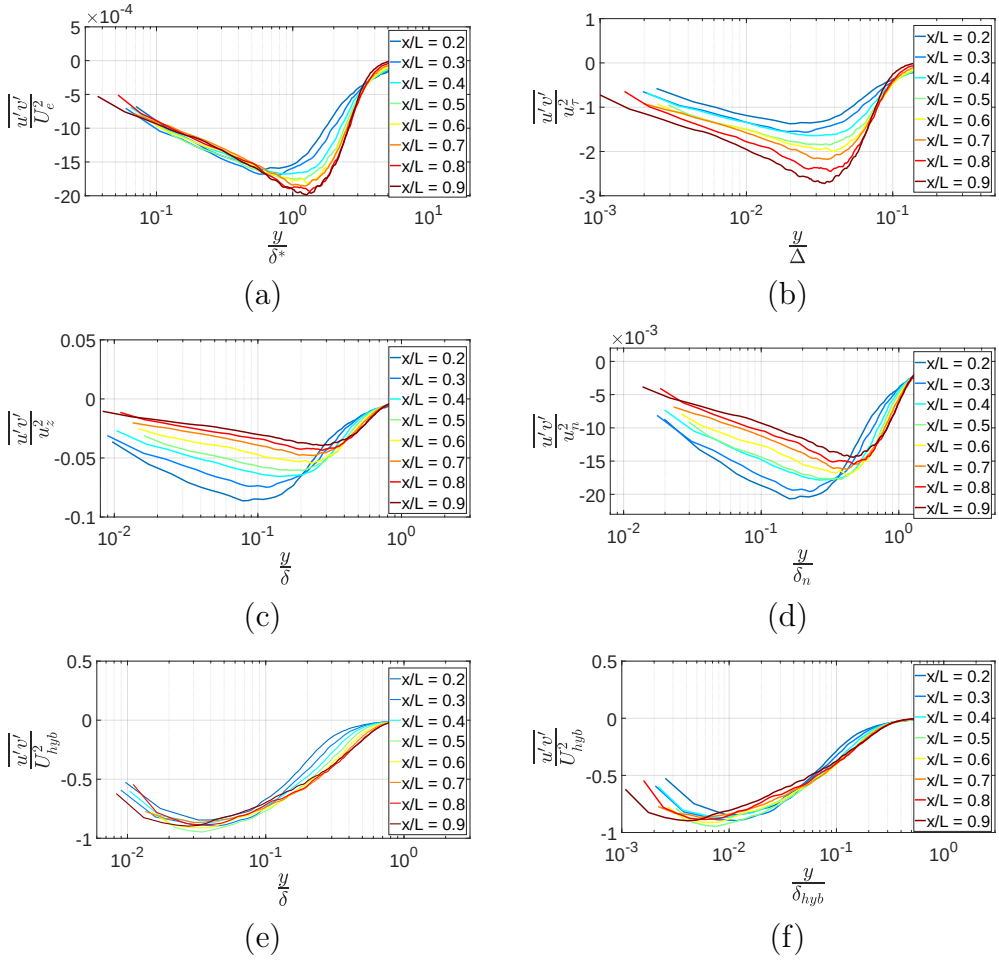

Figure 29: Different scaling of Reynolds shear stress ($\overline{u'v'}$) along the ramp for $-5°$ at 5 m/s. The scaling parameters are from George and Castillo (1997) (a) , Clauser (1956) (b), Zagarola and Smits (1998) (c), Pirozzoli and Smits (2023) (d), Romero et al. (2022) (e) and the present proposition (f).

ity. In contrast, the other scaling parameters provide less accurate representations of the Reynolds shear stress and therefore their results will not be further presented. Nevertheless, we can observe that most of the scaling parameters are more efficient around $x/L = 0.75$ as observed on the mean velocity profiles.

Fig. 30 compares the scaling parameters of Romero et al. (2022) (left) and our new scaling parameters (right) for the $-5°$ plate at 5 m/s. It shows the

profiles of Reynolds stress $\overline{u'u'}$ (i.e. Fig. 30 (a) & (b)), $\overline{v'v'}$ (i.e. Fig. 30 (c) & (d)) and $\overline{u'v'}$ (i.e. Fig. 30 (e) & (f)). Like the scaling of the mean velocity, these scaling methods appear to work effectively across the plate for $0.2 < x/L < 0.9$, with an observable stabilization phenomena as seen before for x/L of the order of 0.75. Our scaling approach shows a slight improvement over Romero's, particularly in the scaling of u'^2 and v'^2.

Fig. 31 illustrates the Reynolds stress scaling for both plates at both speeds as for the mean velocity in Fig. 26. It shows the profiles of Reynolds stress $\overline{u'u'}$ (i.e. Fig. 31 (a) & (b)), $\overline{v'v'}$ (i.e. Fig. 31 (c) & (d)) and $\overline{u'v'}$ (i.e. Fig. 31 (e) & (f)) with the scaling parameters of Romero et al. (2022) (left) and the proposed new scaling parameters (right). We can observe that the two scaling methods groups the curves of each ramp angle and thus eliminates the dependency on the Reynolds number with a little more efficiency for the new scaling. Nevertheless, it does not fully eliminate the influence of the pressure gradient, as the results still show two distinct groups corresponding to the different angles. This could be due to a strong difference in the range of β which cannot be compensated by the scaling or due to a small difference of the history of the flow that could be observed in Fig. 8 when the angles vary.

5. Conclusions

This study presents an in-depth comparison of two experimental data sets to explore the scaling of turbulent boundary layers under the effect of an adverse pressure gradient. By studying the flow over inclined plates at $-5°$ and $-8°$, we sought to characterize the impact of pressure gradients on turbulence structure and mean flow behaviour. The database described in Cuvier et al. (2017) for an APG TBL developing on a flat plate at an angle of $-5°$ is supplemented here by a series of new experiments for an APG TBL developing on a flat plate at an increased angle of $-8°$ using the same upstream flow conditions with essentially the same flow history. Both experiments used advanced PIV techniques to collect high-resolution two-component velocity data, particularly in the outer region of the boundary layer, where traditional turbulence models often struggle to prevail.

The results indicate that, although no scaling approach is universally applicable to the enitre extent of the ramp, significant progress has been made in identifying scaling parameters that are more effective in capturing the flow behaviour, particularly further downstream where the flow is essentially

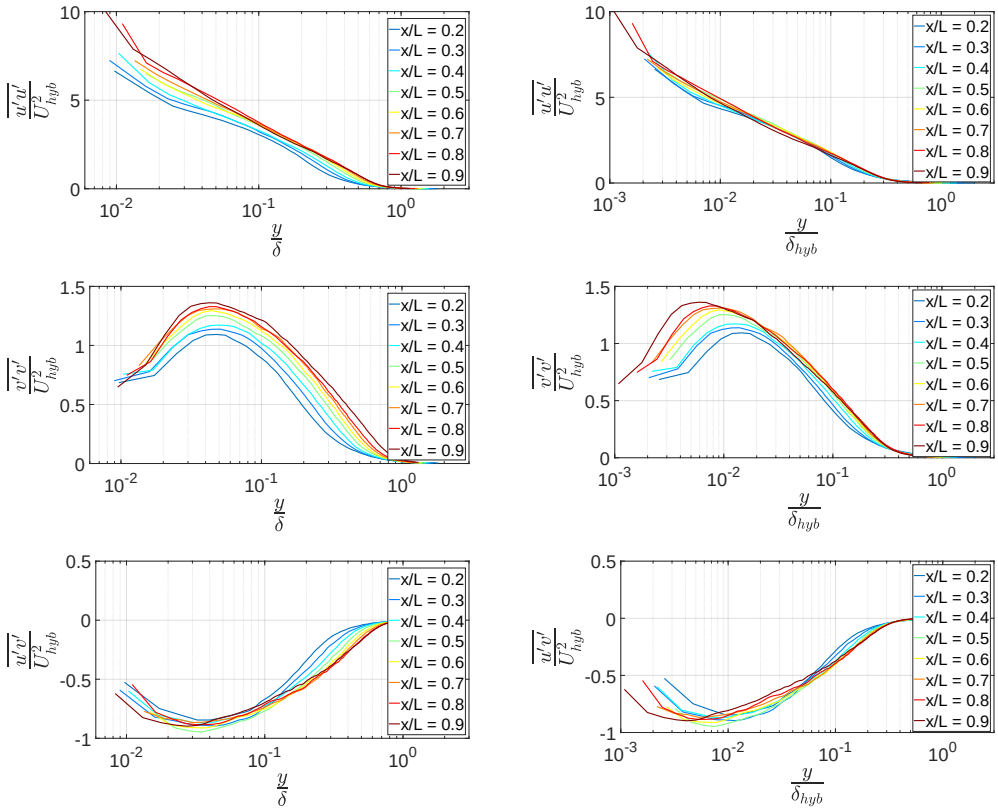

Figure 30: Comparing different scaling of Reynolds stresses ($\overline{u'u'}$) (a) and (b), ($\overline{v'v'}$) (c) and (d), ($\overline{u'v'}$) (e) and (f) along the ramp for $-5°$ at 5 m/s. The scaling parameters are from Romero et al. (2022) (a), (c) and (e) and the present proposition (b), (d) and (f).

fully developed for the specific APG environment. The theoretical approach proposed by Pirozzoli and Smits (2023) and the scaling laws introduced by Romero et al. (2022) appear to give satisfactory results with regard to the mean velocity profile in the outer region. The modifications proposed in this work, based on these two approaches, proved particularly effective in scaling the mean velocity including the Reynolds shear stress. This reinforces the need for a refined approach to modeling turbulence in APG regions, which are critical in many industrial applications.

Moreover, the analysis of Reynolds stresses by comparison of the two experiments revealed the persistence of pressure gradient effects, even after reducing the Reynolds number dependency (see Fig. 31). The experimen-

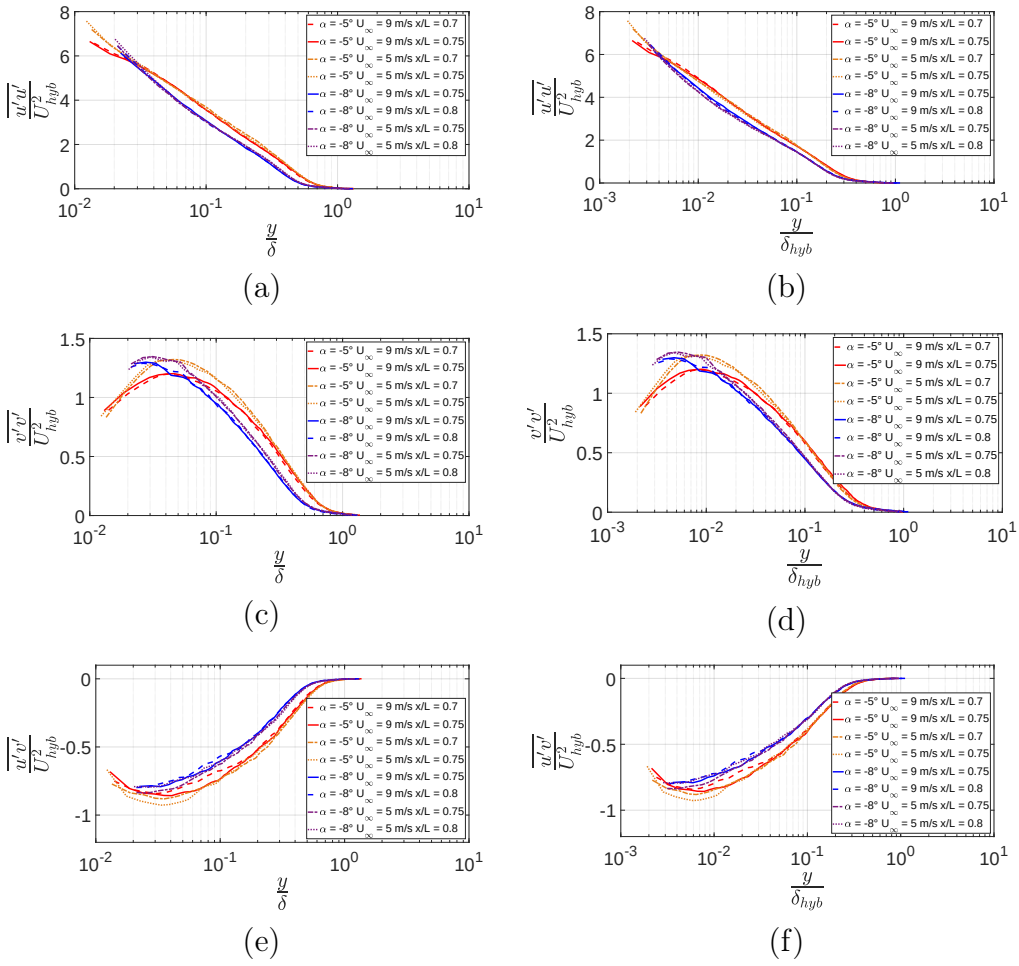

Figure 31: Comparison of different scaling of Reynolds stress ($\overline{u'u'}$) (a) and (b), ($\overline{v'v'}$) (c) and (d), ($\overline{u'v'}$) (e) and (f) for the two different Reynolds numbers and the two angles around $x/L = 0.75$. The scaling parameters are from Romero et al. (2022) (a), (c) and (e) and the present proposition (b), (d) and (f).

tal findings highlight the importance of a continued refinement of scaling laws for APG flows thereby contributing to a better understanding of turbulence in decelerating boundary layers. The data gathered in this study offers a valuable resource for future numerical simulations and model validation, addressing key gaps in the physical understanding of APG turbulence and helping to improve predictive capabilities in complex industrial flows.

In conclusion, this work provides a comprehensive experimental dataset

and insights into the challenges of scaling turbulent boundary layers under APG environments, offering a robust test case for advancing turbulence models and their predictive accuracy.

Supplementary material

The database is available upon request by contacting C. Cuvier (christophe.cuvier@centralelille.fr or J.M. Foucaut (jean-marc.foucaut@centralelille.fr).

Acknowledgements

This work was carried out within the framework of the RITMEA project supported by the European Community, the French Ministry for Higher Education and Research, and the Hauts de France Regional Council in connection with CNRS Research Foundation on Ground Transport and Mobility. The scientific head of ONERA is acknowledged for the support in the frame of the two projects PR Frottement and PR Meteor. The authors would also like to thank Yasar Ostovan for the contribution to the experiments, Laurent Keirsbulk for his contribution during the Corentin's internship and Nicolas Renard for ONERA's scientific interest in them.

References

Bobke, A., Vinuesa, R., Orlu, R., Schlatter, P., 2017. History effects and near equilibrium in adverse-pressure-gradient turbulent boundary layers. J. Fluid Mech. 820, 667–692. doi:10.1017/jfm.2017.236.

Castillo, L., George, W.K., 2001. Similarity analysis for turbulent boundary layer with pressure gradient: Outer flow. AIAA J. 39. doi:10.2514/2.1300.

Chen, P.E.S., Wu, W., Griffin, K.P., Shi, Y., Yang, X.I.A., 2023. A universal velocity transformation for boundary layers with pressure gradients. J. Fluid Mech. 970. doi:10.1017/jfm.2023.570.

Clauser, F.H., 1954. Turbulent boundary layers in adverse pressure gradients. J. Aeronaut. Sci. 21, 91–108. doi:10.2514/8.2938.

Clauser, F.H., 1956. The turbulent boundary layer. Advances Appl. Mech. 4, 1–51. doi:10.1016/S0065-2156(08)70370-3.

Coles, D.E., 1956. The law of the wake in the turbulent boundary layer. J. Fluid Mech. 1, 191–223. doi:doi:10.1017/S0022112056000135.

Coles, D.E., 1968. The young person's guide to the data, in: Thermosciences Division, S.U. (Ed.), AF0SR-IFP-Stanford Conference on Computation of Turbulent Boundary Layers, pp. 1–45. URL: `https://apps.dtic.mil/sti/tr/pdf/AD0695076.pdf`.

Cuvier, C., Foucaut, J.M., Braud, C., Stanislas, M., 2014. Characterization of a high Reynolds number boundary layer subject to pressure gradient and separation. J. Turbul. 15, 473–515. doi:10.1080/14685248.2014.914217.

Cuvier, C., Srinath, S., Stanislas, M., Foucaut, J.M., Laval, J., Kähler, C., Hain, R., Scharnowski, S., Schröder, A., Geisler, R., Agocs, J., Röse, A., Willert, C., Klinner, J., Amili, O., Atkinson, O., J., S., 2017. Extensive characterisation of a high Reynolds number decelerating boundary layer using advanced optical metrology. J. Turbul. 18, 929–972. doi:10.1080/14685248.2017.1342827.

Foucaut, J., Milliat, B., Stanislas, M., 2003. Optimisation de la PIV pour l'étude de la turbulence. analyse de la précision, in: 16ème congrès Français de Mécanique, 1-5 sep.

Foucaut, J.M., Stanislas, M., 2002. Some considerations on the accuracy and frequency response of some derivative filters applied to PIV vector fields. Measurement Science and Technology 13, 1058–1071.

George, W.K., Castillo, L., 1997. Zero-pressure-gradient turbulent boundary layer. Appl. Mech. Rev. 50, 689–729. doi:10.1115/1.3101858.

Gungor, A.G., Maciel, Y., P., S.M., Soria, J., 2017. Direct numerical simulation of a non-equilibrium adverse pressure gradient boundary layer up to $\mathrm{Re}_\theta = 8000$, in: Society, E.M. (Ed.), 16th European Turbulence Conference.

Han, M., Ma, M., Yan, C., 2024. Consistent outer scaling and analysis of adverse pressure gradient turbulent boundary layers. J. Fluid Mech. 982. doi:10.1017/jfm.2024.97.

Harun, Z., Monty, J.P., Mathis, R., Marusic, I., 2013. Pressure gradient effects on the large-scale structure of turbulent boundary layer. J. Fluid Mech. 715, 477–498. doi:10.1017/jfm.2012.531.

Kitsios, V., Sekimoto, A., Atkinson, C., Sillero, J.A., Borrel, G., Gungor, A.G., Jimenez, J., Soria, J., 2017. Direct numerical simulation of a self-similar adverse pressure gradient turbulent boundary layer at the verge of separation. J. Fluid Mech. 829, 392–419. doi:10.1017/jfm.2017.549.

Klewicki, J., Sandberg, R., Knopp, T., Devenport, W., Fritsch, D., Vishwanathan, V., Volino, R., Serge, T., Beverley, M., Luis, E., 2024. On the physical structure, modelling and computation-based prediction of two-dimensional, smooth-wall turbulent boundary layers subjected to streamwise pressure gradients. J. Turbul. 25, 345–368. doi:10.1080/14685248.2024.2392572.

Knopp, T., Buchmann, N.A., Schanz, D., Eisfeld, B., Cierpka, C., Hain, R., Schröder, A., Kähler, C.J., 2015. Investigation of scaling laws in a turbulent boundary layer flow with adverse pressure gradient using PIV. J. Turbul. 16, 250–272. doi:10.1080/14685248.2014.943906.

Lecordier, B., Westerweel, J., 2004. The EUROPIV synthetic image generator (SIG), in: Stanislas, M., Westerweel, J., Kompenhans, J. (Eds.), Particle Image Velocimetry: Recent Improvements, Springer-Verlag Berlin. pp.

145–161. EUROPIV 2 Workshop, Zaragoza, SPAIN, 31 March – 01 April, 2003.

Ludwig, H., Tillman, W., 1950. Investigations of the wall-shearing stress in turbulent boundary layers. Nat. Adv. Comm. Aero. Wash. Tech. Mem. NACA-TM-1285.

Maciel, Y., Rossignol, K.S., Lemay, J., 2006. A study of a turbulent boundary layer in stalled-airfoil-type flow conditions. Exp. Fluids 41, 573–590. doi:10.1007/s00348-006-0182-1.

Maciel, Y., Wei, T., Gungor, A., M.P., S., 2018. Outer scales and parameters of adverse-pressure-gradient turbulent boundary layers. J. Fluid Mech. 844, 5–35. doi:10.1017/jfm.2018.193.

Mellor, G.L., Gibson, D.M., 1966. Equilibrium turbulent boundary layers. J. Fluid Mech. 24, 225–253. doi:10.1017/S0022112066000612.

Monty, J., Harun, Z., Marusic, I., 2011. A parametric study of adverse pressure gradient turbulent boundary layers. Int. J. Heat Fluid Flow 32. doi:10.1016/j.ijheatfluidflow.2011.03.004.

Nagib, H.M., Chauhan, K., 2008. Variations of von karman coefficient in canonical flows. Phys. Fluids 20, 101518. doi:10.1063/1.3006423.

Panton, R.L., 2005. Review of wall turbulence as described by composite expansions. Appl. Mech. Rev. 58, 1–36. doi:10.1115/1.1840903.

Perry, A., 1966. Turbulent boundary layers in decreasing adverse pressure gradients. J. Fluid Mech. 26, 481–506. doi:10.1017/S0022112066001344.

Pirozzoli, S., Smits, A.J., 2023. Outer-layer universality of the mean velocity profile in turbulent wall-bounded flows. Phys. Rev. Fluids 8, 064607. doi:10.1103/PhysRevFluids.8.064607.

Romero, S., Zimmerman, S., Philip, J., Klewicki, J., 2022. Stress equation based scaling framework for adverse pressure gradient turbulent boundary layers. Int. J. Heat Fluid Flow 93. doi:10.1016/j.ijheatfluidflow.2021.108885.

Rotta, J., 1950. Über die Theorie der turbulenten Grenzschichten. Mitteilungen aus dem Max-Planck-Institut für Strömungsforschung. volume 1. Max-Planck-Inst. f. Strömungsforschung, Göttingen. URL: https://ntrs.nasa.gov/citations/19930093886. translated as: On the theory of turbulent boundary layers, NACA-TM-1344, (1953).

Sanmiguel Vila, C., Orlu, R., Vinuesa, R., Schlatter, P., Ianiro, A., Discetti, S., 2017. Adverse-pressure-gradient effects on turbulent boundary layers: Statistics and flow-field organization. Flow Turb. Combust. 99, 589–612. doi:10.1007/s10494-017-9869-z.

Scarano, F., 2002. Iterative image deformation methods in PIV. Meas. Sci. Technol. 13, R1–R19. doi:10.1088/0957-0233/13/1/201.

Soria, J., 1996. An investigation of the near wake of a circular cylinder using a video-based digital cross-correlation particle image velocimetry technique. Exp. Therm. Fluid Sci. 12, 221–233. doi:10.1016/0894-1777(95)00086-0.

Townsend, A.A., 1956. The properties of equilibrium boundary layers. J. Fluid Mech. 1, 561–573. doi:10.1017/S0022112056000378.

Townsend, A.A., 1961. Equilibrium layers and wall turbulence. J. Fluid Mech. 11, 97–120. doi:10.1017/S0022112061000883.

Vinuesa, R., Bobke, A., Orlu, R., Schlatter, P., 2016. On determining characteristic length scales in pressure-gradient turbulent boundary layers. Phys. Fluids 28. doi:10.1063/1.4947532.

Wei, T., Knopp, T., 2023. Outer scaling of the mean momentum equation for turbulent boundary layers under adverse pressure gradient. J. Fluid Mech. 958. doi:10.1017/jfm.2023.72.

Willert, C.E., 2015. High-speed particle image velocimetry for the efficient measurement of turbulence statistics. Exp. Fluids 56, 17. doi:10.1007/s00348-014-1892-4.

Willert, C.E., Gharib, M., 1991. Digital particle image velocimetry. Exp. Fluids 10, 181–193. doi:10.1007/BF00190388.

Zagarola, M.V., Smits, A., 1998. A new mean velocity scaling for turbulent boundary layers, in: Proc. 1998 FEDSM'98 Fluids Engineering Division

Summer Meeting, June 21-25, 1998, Washington DC, ASME, NewYork, NY.